Branching fraction measurements of the color-suppressed decays $\bar{B}^0$ to $D^{(*)0}\pi^0$, $D^{(*)0}\eta$, $D^{(*)0}\omega$, and $D^{(*)0}\eta'$ and measurement of the polarization in the decay $\bar{B}^0 \to D^{*0}\omega$

J. P. Lees,[1] V. Poireau,[1] V. Tisserand,[1] J. Garra Tico,[2] E. Grauges,[2] M. Martinelli,[3a,3b] D. A. Milanes,[3a] A. Palano,[3a,3b] M. Pappagallo,[3a,3b] G. Eigen,[4] B. Stugu,[4] D. N. Brown,[5] L. T. Kerth,[5] Yu. G. Kolomensky,[5] G. Lynch,[5] H. Koch,[6] T. Schroeder,[6] D. J. Asgeirsson,[7] C. Hearty,[7] T. S. Mattison,[7] J. A. McKenna,[7] A. Khan,[8] V. E. Blinov,[9] A. R. Buzykaev,[9] V. P. Druzhinin,[9] V. B. Golubev,[9] E. A. Kravchenko,[9] A. P. Onuchin,[9] S. I. Serednyakov,[9] Yu. I. Skovpen,[9] E. P. Solodov,[9] K. Yu. Todyshev,[9] A. N. Yushkov,[9] M. Bondioli,[10] D. Kirkby,[10] A. J. Lankford,[10] M. Mandelkern,[10] D. P. Stoker,[10] H. Atmacan,[11] J. W. Gary,[11] F. Liu,[11] O. Long,[11] G. M. Vitug,[11] C. Campagnari,[12] T. M. Hong,[12] D. Kovalskyi,[12] J. D. Richman,[12] C. A. West,[12] A. M. Eisner,[13] J. Kroseberg,[13] W. S. Lockman,[13] A. J. Martinez,[13] T. Schalk,[13] B. A. Schumm,[13] A. Seiden,[13] C. H. Cheng,[14] D. A. Doll,[14] B. Echenard,[14] K. T. Flood,[14] D. G. Hitlin,[14] P. Ongmongkolkul,[14] F. C. Porter,[14] A. Y. Rakitin,[14] R. Andreassen,[15] M. S. Dubrovin,[15] Z. Huard,[15] B. T. Meadows,[15] M. D. Sokoloff,[15] L. Sun,[15] P. C. Bloom,[16] W. T. Ford,[16] A. Gaz,[16] M. Nagel,[16] U. Nauenberg,[16] J. G. Smith,[16] S. R. Wagner,[16] R. Ayad,[17,*] W. H. Toki,[17] B. Spaan,[18] M. J. Kobel,[19] X. Prudent,[19] K. R. Schubert,[19] R. Schwierz,[19] D. Bernard,[20] M. Verderi,[20] P. J. Clark,[21] S. Playfer,[21] D. Bettoni,[22a] C. Bozzi,[22a] R. Calabrese,[22a,22b] G. Cibinetto,[22a,22b] E. Fioravanti,[22a,22b] I. Garzia,[22a,22b] E. Luppi,[22a,22b] M. Munerato,[22a,22b] M. Negrini,[22a,22b] L. Piemontese,[22a] V. Santoro,[22a] R. Baldini-Ferroli,[23] A. Calcaterra,[23] R. de Sangro,[23] G. Finocchiaro,[23] M. Nicolaci,[23] P. Patteri,[23] I. M. Peruzzi,[23,†] M. Piccolo,[23] M. Rama,[23] A. Zallo,[23] R. Contri,[24a,24b] E. Guido,[24a,24b] M. Lo Vetere,[24a,24b] M. R. Monge,[24a,24b] S. Passaggio,[24a] C. Patrignani,[24a,24b] E. Robutti,[24a] B. Bhuyan,[25] V. Prasad,[25] C. L. Lee,[26] M. Morii,[26] A. J. Edwards,[27] A. Adametz,[28] J. Marks,[28] U. Uwer,[28] F. U. Bernlochner,[29] M. Ebert,[29] H. M. Lacker,[29] T. Lueck,[29] P. D. Dauncey,[30] M. Tibbetts,[30] P. K. Behera,[31] U. Mallik,[31] C. Chen,[32] J. Cochran,[32] W. T. Meyer,[32] S. Prell,[32] E. I. Rosenberg,[32] A. E. Rubin,[32] A. V. Gritsan,[33] Z. J. Guo,[33] N. Arnaud,[34] M. Davier,[34] G. Grosdidier,[34] F. Le Diberder,[34] A. M. Lutz,[34] B. Malaescu,[34] P. Roudeau,[34] M. H. Schune,[34] A. Stocchi,[34] G. Wormser,[34] D. J. Lange,[35] D. M. Wright,[35] I. Bingham,[36] C. A. Chavez,[36] J. P. Coleman,[36] J. R. Fry,[36] E. Gabathuler,[36] D. E. Hutchcroft,[36] D. J. Payne,[36] C. Touramanis,[36] A. J. Bevan,[37] F. Di Lodovico,[37] R. Sacco,[37] M. Sigamani,[37] G. Cowan,[38] D. N. Brown,[39] C. L. Davis,[39] A. G. Denig,[40] M. Fritsch,[40] W. Gradl,[40] A. Hafner,[40] E. Prencipe,[40] K. E. Alwyn,[41] D. Bailey,[41] R. J. Barlow,[41,‡] G. Jackson,[41] G. D. Lafferty,[41] R. Cenci,[42] B. Hamilton,[42] A. Jawahery,[42] D. A. Roberts,[42] G. Simi,[42] C. Dallapiccola,[43] R. Cowan,[44] D. Dujmic,[44] G. Sciolla,[44] D. Lindemann,[45] P. M. Patel,[45] S. H. Robertson,[45] M. Schram,[45] P. Biassoni,[46a,46b] A. Lazzaro,[46a,46b] V. Lombardo,[46a] N. Neri,[46a,46b] F. Palombo,[46a,46b] S. Stracka,[46a,46b] L. Cremaldi,[47] R. Godang,[47,§] R. Kroeger,[47] P. Sonnek,[47] D. J. Summers,[47] X. Nguyen,[48] P. Taras,[48] G. De Nardo,[49a,49b] D. Monorchio,[49a,49b] G. Onorato,[49a,49b] C. Sciacca,[49a,49b] G. Raven,[50] H. L. Snoek,[50] C. P. Jessop,[51] K. J. Knoepfel,[51] J. M. LoSecco,[51] W. F. Wang,[51] K. Honscheid,[52] R. Kass,[52] J. Brau,[53] R. Frey,[53] N. B. Sinev,[53] D. Strom,[53] E. Torrence,[53] E. Feltresi,[54a,54b] N. Gagliardi,[54a,54b] M. Margoni,[54a,54b] M. Morandin,[54a] M. Posocco,[54a] M. Rotondo,[54a] F. Simonetto,[54a,54b] R. Stroili,[54a,54b] E. Ben-Haim,[55] M. Bomben,[55] G. R. Bonneaud,[55] H. Briand,[55] G. Calderini,[55] J. Chauveau,[55] O. Hamon,[55] Ph. Leruste,[55] G. Marchiori,[55] J. Ocariz,[55] S. Sitt,[55] M. Biasini,[56a,56b] E. Manoni,[56a,56b] S. Pacetti,[56a,56b] A. Rossi,[56a,56b] C. Angelini,[57a,57b] G. Batignani,[57a,57b] S. Bettarini,[57a,57b] M. Carpinelli,[57a,57b,‖] G. Casarosa,[57a,57b] A. Cervelli,[57a,57b] F. Forti,[57a,57b] M. A. Giorgi,[57a,57b] A. Lusiani,[57a,57c] B. Oberhof,[57a,57b] E. Paoloni,[57a,57b] A. Perez,[57a] G. Rizzo,[57a,57b] J. J. Walsh,[57a] D. Lopes Pegna,[58] C. Lu,[58] J. Olsen,[58] A. J. S. Smith,[58] A. V. Telnov,[58] F. Anulli,[59a,59b] G. Cavoto,[59a] R. Faccini,[59a,59b] F. Ferrarotto,[59a] F. Ferroni,[59a,59b] M. Gaspero,[59a,59b] L. Li Gioi,[59a] M. A. Mazzoni,[59a] G. Piredda,[59a] C. Bünger,[60] O. Grünberg,[60] T. Hartmann,[60] T. Leddig,[60] H. Schröder,[60] R. Waldi,[60] T. Adye,[61] E. O. Olaiya,[61] F. F. Wilson,[61] S. Emery,[62] G. Hamel de Monchenault,[62] G. Vasseur,[62] Ch. Yèche,[62] D. Aston,[63] D. J. Bard,[63] R. Bartoldus,[63] C. Cartaro,[63] M. R. Convery,[63] J. Dorfan,[63] G. P. Dubois-Felsmann,[63] W. Dunwoodie,[63] R. C. Field,[63] M. Franco Sevilla,[63] B. G. Fulsom,[63] A. M. Gabareen,[63] M. T. Graham,[63] P. Grenier,[63] C. Hast,[63] W. R. Innes,[63] M. H. Kelsey,[63] H. Kim,[63] P. Kim,[63] M. L. Kocian,[63] D. W. G. S. Leith,[63] P. Lewis,[63] S. Li,[63] B. Lindquist,[63] S. Luitz,[63] V. Luth,[63] H. L. Lynch,[63] D. B. MacFarlane,[63] D. R. Muller,[63] H. Neal,[63] S. Nelson,[63] I. Ofte,[63] M. Perl,[63] T. Pulliam,[63] B. N. Ratcliff,[63] A. Roodman,[63] A. A. Salnikov,[63] R. H. Schindler,[63] A. Snyder,[63] D. Su,[63] M. K. Sullivan,[63] J. Va'vra,[63] A. P. Wagner,[63] M. Weaver,[63] W. J. Wisniewski,[63] M. Wittgen,[63] D. H. Wright,[63] H. W. Wulsin,[63] A. K. Yarritu,[63] C. C. Young,[63] V. Ziegler,[63] W. Park,[64] M. V. Purohit,[64] R. M. White,[64] J. R. Wilson,[64] A. Randle-Conde,[65] S. J. Sekula,[65] M. Bellis,[66] J. F. Benitez,[66] P. R. Burchat,[66] T. S. Miyashita,[66] M. S. Alam,[67] J. A. Ernst,[67] R. Gorodeisky,[68] N. Guttman,[68] D. R. Peimer,[68] A. Soffer,[68] P. Lund,[69] S. M. Spanier,[69] R. Eckmann,[70] J. L. Ritchie,[70] A. M. Ruland,[70] C. J. Schilling,[70] R. F. Schwitters,[70] B. C. Wray,[70] J. M. Izen,[a71] X. C. Lou,[a71] F. Bianchi,[72a,72b] D. Gamba,[72a,72b]

L. Lanceri,[73a,73b] L. Vitale,[73a,73b] F. Martinez-Vidal,[74] A. Oyanguren,[74] H. Ahmed,[75] J. Albert,[75] Sw. Banerjee,[75] H. H. F. Choi,[75] G. J. King,[75] R. Kowalewski,[75] M. J. Lewczuk,[75] C. Lindsay,[75] I. M. Nugent,[75] J. M. Roney,[75] R. J. Sobie,[75] N. Tasneem,[75] T. J. Gershon,[76] P. F. Harrison,[76] T. E. Latham,[76] E. M. T. Puccio,[76] H. R. Band,[77] S. Dasu,[77] Y. Pan,[77] R. Prepost,[77] and S. L. Wu[77]

(The *BABAR* Collaboration)

[1]*Laboratoire d'Annecy-le-Vieux de Physique des Particules (LAPP), Université de Savoie, CNRS/IN2P3, F-74941 Annecy-Le-Vieux, France*
[2]*Universitat de Barcelona, Facultat de Fisica, Departament ECM, E-08028 Barcelona, Spain*
[3a]*INFN Sezione di Bari, Dipartimento di Fisica, I-70126 Bari, Italy*
[3b]*Dipartimento di Fisica, Università di Bari, I-70126 Bari, Italy*
[4]*University of Bergen, Institute of Physics, N-5007 Bergen, Norway*
[5]*Lawrence Berkeley National Laboratory and University of California, Berkeley, California 94720, USA*
[6]*Ruhr Universität Bochum, Institut für Experimentalphysik 1, D-44780 Bochum, Germany*
[7]*University of British Columbia, Vancouver, British Columbia, Canada V6T 1Z1*
[8]*Brunel University, Uxbridge, Middlesex UB8 3PH, United Kingdom*
[9]*Budker Institute of Nuclear Physics, Novosibirsk 630090, Russia*
[10]*University of California at Irvine, Irvine, California 92697, USA*
[11]*University of California at Riverside, Riverside, California 92521, USA*
[12]*University of California at Santa Barbara, Santa Barbara, California 93106, USA*
[13]*University of California at Santa Cruz, Institute for Particle Physics, Santa Cruz, California 95064, USA*
[14]*California Institute of Technology, Pasadena, California 91125, USA*
[15]*University of Cincinnati, Cincinnati, Ohio 45221, USA*
[16]*University of Colorado, Boulder, Colorado 80309, USA*
[17]*Colorado State University, Fort Collins, Colorado 80523, USA*
[18]*Technische Universität Dortmund, Fakultät Physik, D-44221 Dortmund, Germany*
[19]*Technische Universität Dresden, Institut für Kern- und Teilchenphysik, D-01062 Dresden, Germany*
[20]*Laboratoire Leprince-Ringuet, Ecole Polytechnique, CNRS/IN2P3, F-91128 Palaiseau, France*
[21]*University of Edinburgh, Edinburgh EH9 3JZ, United Kingdom*
[22a]*INFN Sezione di Ferrara, Dipartimento di Fisica, I-44100 Ferrara, Italy*
[22b]*Dipartimento di Fisica, Università di Ferrara, I-44100 Ferrara, Italy*
[23]*INFN Laboratori Nazionali di Frascati, I-00044 Frascati, Italy*
[24a]*INFN Sezione di Genova, Dipartimento di Fisica, I-16146 Genova, Italy*
[24b]*INFN Sezione di Genova, Università di Genova, I-16146 Genova, Italy*
[25]*Indian Institute of Technology Guwahati, Guwahati, Assam, 781 039, India*
[26]*Harvard University, Cambridge, Massachusetts 02138, USA*
[27]*Harvey Mudd College, Claremont, California 91711*
[28]*Universität Heidelberg, Physikalisches Institut, Philosophenweg 12, D-69120 Heidelberg, Germany*
[29]*Humboldt-Universität zu Berlin, Institut für Physik, Newtonstr. 15, D-12489 Berlin, Germany*
[30]*Imperial College London, London, SW7 2AZ, United Kingdom*
[31]*University of Iowa, Iowa City, Iowa 52242, USA*
[32]*Iowa State University, Ames, Iowa 50011-3160, USA*
[33]*Johns Hopkins University, Baltimore, Maryland 21218, USA*
[34]*Laboratoire de l'Accélérateur Linéaire, IN2P3/CNRS et Université Paris-Sud 11, Centre Scientifique d'Orsay, B. P. 34, F-91898 Orsay Cedex, France*
[35]*Lawrence Livermore National Laboratory, Livermore, California 94550, USA*
[36]*University of Liverpool, Liverpool L69 7ZE, United Kingdom*
[37]*Queen Mary, University of London, London, E1 4NS, United Kingdom*
[38]*University of London, Royal Holloway and Bedford New College, Egham, Surrey TW20 0EX, United Kingdom*
[39]*University of Louisville, Louisville, Kentucky 40292, USA*
[40]*Johannes Gutenberg-Universität Mainz, Institut für Kernphysik, D-55099 Mainz, Germany*

[*]Now at Temple University, Philadelphia, PA 19122, USA
[†]Also with Università di Perugia, Dipartimento di Fisica, Perugia, Italy
[‡]Now at the University of Huddersfield, Huddersfield HD1 3DH, UK
[§]Now at University of South Alabama, Mobile, AL 36688, USA
[‖]Also with Università di Sassari, Sassari, Italy

[41]University of Manchester, Manchester M13 9PL, United Kingdom
[42]University of Maryland, College Park, Maryland 20742, USA
[43]University of Massachusetts, Amherst, Massachusetts 01003, USA
[44]Massachusetts Institute of Technology, Laboratory for Nuclear Science, Cambridge, Massachusetts 02139, USA
[45]McGill University, Montréal, Québec, Canada H3A 2T8
[46a]INFN Sezione di Milano, Dipartimento di Fisica, I-20133 Milano, Italy
[46b]Dipartimento di Fisica, Università di Milano, I-20133 Milano, Italy
[47]University of Mississippi, University, Mississippi 38677, USA
[48]Université de Montréal, Physique des Particules, Montréal, Québec, Canada H3C 3J7
[49a]INFN Sezione di Napoli, Dipartimento di Scienze Fisiche, I-80126 Napoli, Italy
[49b]Dipartimento di Scienze Fisiche, Università di Napoli Federico II, I-80126 Napoli, Italy
[50]NIKHEF, National Institute for Nuclear Physics and High Energy Physics, NL-1009 DB Amsterdam, The Netherlands
[51]University of Notre Dame, Notre Dame, Indiana 46556, USA
[52]Ohio State University, Columbus, Ohio 43210, USA
[53]University of Oregon, Eugene, Oregon 97403, USA
[54a]INFN Sezione di Padova, Dipartimento di Fisica, I-35131 Padova, Italy
[54b]Dipartimento di Fisica, Università di Padova, I-35131 Padova, Italy
[55]Laboratoire de Physique Nucléaire et de Hautes Energies, IN2P3/CNRS, Université Pierre et Marie Curie-Paris6, Université Denis Diderot-Paris7, F-75252 Paris, France
[56a]INFN Sezione di Perugia, Dipartimento di Fisica, I-06100 Perugia, Italy
[56b]Dipartimento di Fisica, Università di Perugia, I-06100 Perugia, Italy
[57a]INFN Sezione di Pisa, Dipartimento di Fisica, I-56127 Pisa, Italy
[57b]Dipartimento di Fisica, Università di Pisa, I-56127 Pisa, Italy
[57c]Dipartimento di Fisica, Scuola Normale Superiore di Pisa, I-56127 Pisa, Italy
[58]Princeton University, Princeton, New Jersey 08544, USA
[59a]INFN Sezione di Roma, Dipartimento di Fisica, I-00185 Roma, Italy
[59b]Dipartimento di Fisica, Università di Roma La Sapienza, I-00185 Roma, Italy
[60]Universität Rostock, D-18051 Rostock, Germany
[61]Rutherford Appleton Laboratory, Chilton, Didcot, Oxon, OX11 0QX, United Kingdom
[62]CEA, Irfu, SPP, Centre de Saclay, F-91191 Gif-sur-Yvette, France
[63]SLAC National Accelerator Laboratory, Stanford, California 94309 USA
[64]University of South Carolina, Columbia, South Carolina 29208, USA
[65]Southern Methodist University, Dallas, Texas 75275, USA
[66]Stanford University, Stanford, California 94305-4060, USA
[67]State University of New York, Albany, New York 12222, USA
[68]Tel Aviv University, School of Physics and Astronomy, Tel Aviv, 69978, Israel
[69]University of Tennessee, Knoxville, Tennessee 37996, USA
[70]University of Texas at Austin, Austin, Texas 78712, USA
[a71]University of Texas at Dallas, Richardson, Texas 75083, USA
[72a]INFN Sezione di Torino, Dipartimento di Fisica Sperimentale, I-10125 Torino, Italy
[72b]Dipartimento di Fisica Sperimentale, Università di Torino, I-10125 Torino, Italy
[73a]INFN Sezione di Trieste, Dipartimento di Fisica, I-34127 Trieste, Italy
[73b]Dipartimento di Fisica, Università di Trieste, I-34127 Trieste, Italy
[74]IFIC, Universitat de Valencia-CSIC, E-46071 Valencia, Spain
[75]University of Victoria, Victoria, British Columbia, Canada V8W 3P6
[76]Department of Physics, University of Warwick, Coventry CV4 7AL, United Kingdom
[77]University of Wisconsin, Madison, Wisconsin 53706, USA

(Received 29 July 2011; published 16 December 2011)

We report updated branching fraction measurements of the color-suppressed decays $\bar{B}^0 \to D^0\pi^0$, $D^{*0}\pi^0$, $D^0\eta$, $D^{*0}\eta$, $D^0\omega$, $D^{*0}\omega$, $D^0\eta'$, and $D^{*0}\eta'$. We measure the branching fractions ($\times 10^{-4}$): $\mathcal{B}(\bar{B}^0 \to D^0\pi^0) = 2.69 \pm 0.09 \pm 0.13$, $\mathcal{B}(\bar{B}^0 \to D^{*0}\pi^0) = 3.05 \pm 0.14 \pm 0.28$, $\mathcal{B}(\bar{B}^0 \to D^0\eta) = 2.53 \pm 0.09 \pm 0.11$, $\mathcal{B}(\bar{B}^0 \to D^{*0}\eta) = 2.69 \pm 0.14 \pm 0.23$, $\mathcal{B}(\bar{B}^0 \to D^0\omega) = 2.57 \pm 0.11 \pm 0.14$, $\mathcal{B}(\bar{B}^0 \to D^{*0}\omega) = 4.55 \pm 0.24 \pm 0.39$, $\mathcal{B}(\bar{B}^0 \to D^0\eta') = 1.48 \pm 0.13 \pm 0.07$, and $\mathcal{B}(\bar{B}^0 \to D^{*0}\eta') = 1.49 \pm 0.22 \pm 0.15$. We also present the first measurement of the longitudinal polarization fraction of the decay channel $D^{*0}\omega$, $f_L = (66.5 \pm 4.7 \pm 1.5)\%$. In the above, the first uncertainty is statistical and the second is systematic. The results are based on a sample of $(454 \pm 5) \times 10^6$ $B\bar{B}$ pairs collected at the $\Upsilon(4S)$ resonance, with the *BABAR* detector at the PEP-II storage rings at SLAC. The measurements are the most precise determinations of these quantities from a single experiment. They are compared to theoretical predictions obtained by factorization, Soft Collinear Effective Theory (SCET) and perturbative

QCD (pQCD). We find that the presence of final state interactions is favored and the measurements are in better agreement with SCET than with pQCD.

DOI: 10.1103/PhysRevD.84.112007 PACS numbers: 13.25.Hw, 11.30.Er, 12.15.Hh

I. INTRODUCTION

Weak decays of hadrons provide direct access to the parameters of the Cabibbo-Kobayashi-Maskawa (CKM) matrix and thus to the study of CP violation. Strong interaction scattering in the final state [1] (Final State Interactions, or FSI) can modify the decay dynamics and must be well understood. The two-body hadronic B decays with a charmed final state, $B \to D^{(*)}h$, where h is a light meson, are of great help in studying strong-interaction physics related to the confinement of quarks and gluons in hadrons.

The decays $B \to D^{(*)}h$ can proceed through the emission of a $W^{\pm}$ boson following three possible diagrams: external, internal (see Fig. 1), or by a $W^{\pm}$ boson exchange whose contribution to the decay rate is expected to be much smaller than the external and internal amplitudes [2]. The neutral $\bar{B}^0 \to D^{(*)0}h^0$ decays proceed through the internal diagrams [3]. Since mesons are color singlet objects, the quarks from the $W^{\pm}$ decay are constrained to have the anticolor of the spectator quark, which induces a suppression of internal diagrams. For this reason, internal diagrams are called *color-suppressed* and external ones are called *color-allowed*.

We already discussed factorization models [3–6] in our previous publication [7]. Within that approach the nonfactorizable interactions in the final state by soft gluons are neglected. The matrix element in the effective weak Hamiltonian of the decay $B \to D^{(*)}h$ is then factorized into a product of asymptotic states. Factorization appears to be successful in the description of the color-allowed decays [8].

The color-suppressed $b \to c$ decays $\bar{B}^0 \to D^{(*)0}\pi^0$ were first observed by Belle [9] and CLEO [10] with 23.1×10^6 and 9.67×10^6 $B\bar{B}$ pairs, respectively. Belle has also observed the decays $D^0\eta$ and $D^0\omega$ and put upper limits on the branching fraction ($\mathcal{B}$) of $D^{*0}\eta$ and $D^{*0}\omega$ [9]. The

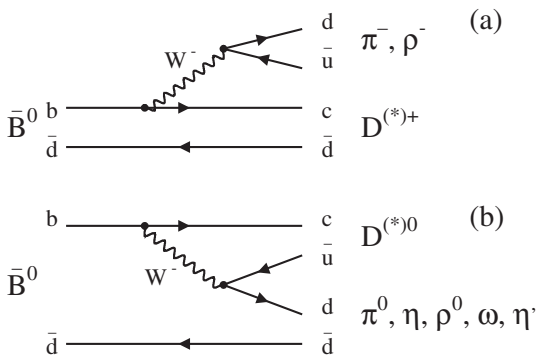

FIG. 1. External (a) and internal (b) tree diagrams for $\bar{B}^0 \to D^{(*)}h$ decays.

branching fraction of the color-suppressed decays $\bar{B}^0 \to D^{(*)0}\pi^0$, $D^{(*)0}\eta$, $D^{(*)0}\omega$, and $D^0\eta'$ were measured by *BABAR* [7] with $88 \times 10^6 B\bar{B}$ pairs and an upper limit was set on $\mathcal{B}(\bar{B}^0 \to D^{*0}\eta')$. Belle updated with $152 \times 10^6 B\bar{B}$ pairs the measurement of $\mathcal{B}(\bar{B}^0 \to D^{(*)0}h^0)$, $h^0 = \pi^0$, η, ω [11], and η' [12] and studied the decays $\bar{B}^0 \to D^0\rho^0$ with $388 \times 10^6 B\bar{B}$ pairs [13]. In an alternative approach, *BABAR* [14] used the charmless neutral B to $K^{\pm}\pi^{\mp}\pi^0$ Dalitz-plot analysis with $232 \times 10^6 B\bar{B}$ pairs, and found $\mathcal{B}(\bar{B}^0 \to D^0\pi^0)$ to be in excellent agreement with earlier experimental results. *BABAR* has also performed a preliminary Dalitz-plot analysis of the mode $B^0 \to \bar{D}^0\pi^+\pi^-$ with $471 \times 10^6 B\bar{B}$ pairs [15].

Many of these branching fraction measurements are significantly larger than predictions obtained within the factorization approximation [3,16]. But, while the initial various experimental results demonstrated overall good consistency, the most recent measurements published by Belle [11,12] have moved on average towards lower $\mathcal{B}$ for the color-suppressed $\bar{B}^0 \to D^{(*)0}h^0$ decays, closer to factorization predictions. However, it has been demonstrated [17] that nonfactorizable contributions are mostly dominant for the color-suppressed charmed $\bar{B}^0 \to D^0\pi^0$ decay and therefore cannot be neglected.

Stronger experimental constraints are therefore needed to distinguish between the different models of the color-suppressed dynamics like pQCD (*perturbative QCD*) [18,19] or SCET (*Soft Collinear Effective Theory*) [20–22]. Finally, we emphasize the need for accurate measurements of hadronic color-suppressed $\bar{B}^0 \to D^{(*)0}h^0$ decays to constrain the theoretical predictions on $\bar{B}_{u,d,s}$ decays to $D^{(*)}P$ and $\bar{D}^{(*)}P$ states, where P is a light pseudoscalar meson such as a pion or a kaon [23]. Using flavor $SU(3)$ symmetry, the comparison of B_d and B_s decays offers new possibilities to determine the decay constant ratio f_s/f_d [23]. These decays are and will be employed to extract the CKM-angle γ and other angles [24], especially in the context of the B-physics program at the LHC.

This paper reports improved branching fraction measurements of eight color-suppressed decays $\bar{B}^0 \to D^{(*)0}\pi^0$, $D^{(*)0}\eta$, $D^{(*)0}\omega$, and $D^{(*)0}\eta'$ with $454 \times 10^6 B\bar{B}$ pairs and presents for the first time the measurement of the longitudinal polarization for the decay mode to two vector mesons $\bar{B}^0 \to D^{*0}\omega$, which also constrains QCD models and challenges *Heavy Quark Effective Theory* (HQET) (see Sec. VI).

II. THE *BABAR* DETECTOR AND DATA SAMPLE

The data used in this analysis were collected with the *BABAR* detector at the PEP-II asymmetric-energy e^+e^-

storage rings operating at SLAC. The *BABAR* detector is described in detail in Ref. [25]. Charged particle tracks are reconstructed using a five-layer silicon vertex tracker (SVT) and a 40-layer drift chamber (DCH) immersed in a 1.5 T magnetic field. Tracks are identified as pions or kaons (particle identification or PID) based on likelihoods constructed from energy loss measurements in the SVT and the DCH and from Cherenkov radiation angles measured in the detector of internally reflected Cherenkov light (DIRC). Photons are reconstructed from showers measured in the CsI(Tl) crystal electromagnetic calorimeter (EMC). Muon and neutral hadron identification is performed with the instrumented flux return (IFR).

The results presented are based on a data sample of an integrated luminosity of 413 fb^{-1} recorded from 1999 to 2007 at the $\Upsilon(4S)$ resonance with a e^+e^- center-of-mass (CM) energy of 10.58 GeV, corresponding to $(454 \pm 5) \times 10^6 B\bar{B}$ pairs. The equal production rate of $B^0\bar{B}^0$ and B^+B^- at that resonance is assumed in this paper, as suggested by the Particle Data Group (PDG) [26]. A data sample of 41.2 fb^{-1} with a CM energy of 10.54 GeV, below the $B\bar{B}$ threshold, is used to study background contributions from continuum events $e^+e^- \to q\bar{q}$ ($q = u, d, s, c$). We call that latter dataset *off-peak events* in what follows.

Samples of simulated Monte Carlo (MC) events are used to determine signal and background characteristics, to optimize selection criteria and to evaluate efficiencies. Simulated events $e^+e^- \to \Upsilon(4S) \to B^+B^-$, $B^0\bar{B}^0$, $e^+e^- \to q\bar{q}$ ($q = u, d, s$) and $e^+e^- \to c\bar{c}$ are generated with *EvtGen* [27], which interfaces to *Pythia* [28] and *Jetset* [29]. Separate samples of exclusive $\bar{B}^0 \to D^{(*)0}h^0$ decays are generated to study the signal features and to quantify the signal selection efficiencies. We also use high statistics control samples of exclusive decays $B^- \to D^{(*)0}\pi^-$ and $D^{(*)0}\rho^-$ for specific selection and background studies. We study these control samples both in data and in the MC, using the same selection criteria. All MC samples include simulation of the *BABAR* detector response generated through *Geant4* [30]. The equivalent integrated luminosity of the MC samples is about 3 times that of the data for $B\bar{B}$, one time for $e^+e^- \to q\bar{q}$ ($q = u, d, s$) and twice for $e^+e^- \to c\bar{c}$ respectively. The equivalent integrated luminosities of the exclusive B decay mode simulations range from 50 to 2500 times the dataset.

III. ANALYSIS METHOD

A. General considerations

The color-suppressed $\bar{B}^0$ meson decay modes are reconstructed from $D^{(*)0}$ meson candidates that are combined with light neutral-meson candidates h^0 (π^0, η, ω, and η'). The $D^{(*)0}$ and h^0 mesons are detected in various possible decay channels. In total, we consider 72 different $\bar{B}^0 \to D^{(*)0}h^0$ decay modes.

We perform a blind analysis: the optimization of the various event selections, the background characterizations and rejections, the efficiency calculations, and most of the systematic uncertainty computations are based on studies done with MC simulations, data sidebands, or data control samples. The fits to data, including the various signal regions, are only performed after all analysis procedures are fixed and systematic uncertainties are studied.

Intermediate particles of the decays $\bar{B}^0 \to D^{(*)0}h^0$ are reconstructed by combining tracks and/or photons for the decay channels with the highest decay rate and detection efficiency. Vertex constraints are applied to charged daughter particles before computing their invariant masses. At each step in the decay chain we require that the candidate mesons have masses consistent with their assumed particle type. If daughter particles are produced in the decay of a parent meson with a natural width that is small relative to the reconstructed width, we constrain the mass of this meson to its nominal value, except for the ω and the ρ^0 [26]. The $\bar{B}^0$ mass is computed using the constraint of the beam energy (see Sec. III C 1). This fitting technique improves the resolution of the energy and the momentum of the $\bar{B}^0$ candidates as they are calculated from improved energies and momenta of the $D^{(*)0}$ and h^0.

Charged particle tracks are reconstructed from measurements in the SVT and/or the DCH, and they are assigned various particle identification probabilities by the PID algorithms. Extrapolated tracks must be in the vicinity of the e^+e^- interaction point, *i.e.* within 1.5 cm in the plane transverse to the beam axis and 2.5 cm along the beam axis. The charged tracks used for the reconstruction of $\eta \to \pi^+\pi^-\pi^0$ and $\eta' \to \pi^+\pi^-\eta(\to \gamma\gamma)$ must in addition have a transverse momentum p_T larger than 100 MeV/c and at least 12 hits in the DCH. When a PID positive identification is required for a track, the track polar angle θ must be in the DIRC fiducial region $25.78° < \theta < 146.10°$. Photons are defined as single clusters of energy deposition in the EMC crystals not matched to a track, and with shower lateral shape consistent with photons. Because of the high machine background in the very forward part of the EMC, we reject photons detected in the region $\theta < 21.19°$. We assume that the production point of the photons is the reconstructed primary vertex of each e^+e^- collision.

The selections applied to each meson (π^0, η, ω, η', D^0, and D^{*0}) are optimized by maximizing the figure of merit $S/\sqrt{S+B}$, where S is the number of signal and B is the number of background events. The numbers S and B are computed from simulations, and the branching ratios used to evaluate S are the present world average values of color-suppressed decay modes [26]. Each particle mass distribution is fitted with a set of Gaussian functions or a so-called *modified Novosibirsk* empirical function [31], which is composed of a Gaussian-like peaking part with two tails at low and high values. Particle candidates are then required to have a mass within $\pm 2.5\sigma$ around the fitted mass central value, where σ is the resolution of the mass distribution obtained by the fit. For the decays $D^0 \to K^-\pi^+\pi^0$

and $D^{*0} \to D^0\gamma$, the lower bound is extended to 3σ because of the photon energy losses in front of and between the EMC crystals, which makes the mass distribution asymmetric with a tail at low values.

B. Selection of intermediate particles

1. π^0 selection

The π^0 mesons are reconstructed from photon pairs. Each photon energy $E\gamma$ must be greater than 85 MeV for π^0 produced directly from B^0 decays, and greater than 60 MeV for π^0 from η, ω, or D^0 meson decays. Slow neutral pions originating from $D^{*0} \to D^0\pi^0$ decays must satisfy $E\gamma > 30$ MeV. The π^0 reconstructed mass resolution ranges 6.5–7.0 MeV/c^2 for π^0 from η, ω, and D^0 mesons decays, and 7.0–7.5 MeV/c^2 for π^0 produced in D^{*0} or B^0 decays.

2. η selection

The η mesons are reconstructed in the $\gamma\gamma$ and $\pi^+\pi^-\pi^0$ decay modes, accounting for about 62% of the total decay rate [26], and may originate from $\bar{B}^0 \to D^{(*)0}\eta$ or $\eta' \to \pi^+\pi^-\eta$ decays.

The $\eta \to \gamma\gamma$ candidates are reconstructed by combining two photons that satisfy $E\gamma > 200$ MeV for $\bar{B}^0$ daughters and $E\gamma > 180$ MeV for η' daughters. As photons originating from high momentum π^0 mesons may fake a $\eta \to \gamma\gamma$ signal, a veto is applied. The $\eta \to \gamma\gamma$ candidate is rejected if either photon combined with any other photon in the event with $E\gamma > 200$ MeV has an invariant mass between 115 and 150 MeV/c^2. Such a veto retains 93% of the signal while reducing the background of fake η mesons candidates by a factor of 2. The resolution of the $\eta \to \gamma\gamma$ mass distribution is approximately 15 MeV/c^2, dominated by the resolution on the photon energy measurement in the EMC.

For η candidates reconstructed in the decay channel $\pi^+\pi^-\pi^0$, the π^0 is required to satisfy the conditions described in Sec. III B 1. The mass resolution is about 3 MeV/c^2, which is better than for the mode $\eta \to \gamma\gamma$, thanks to the relatively better resolution of the tracking system and the various vertex and mass constraints applied to the η and π^0 candidates.

3. ω selection

The ω mesons are reconstructed in the $\pi^+\pi^-\pi^0$ decay mode. This mode accounts for approximately 89% of the total decay rate. The π^0 is required to satisfy the conditions described in Sec. III B 1 and the transverse momenta of the charged pions must be greater than 200 MeV/c. The natural width of the ω mass distribution $\Gamma = 8.49$ MeV [26] is comparable to the experimental resolution $\sigma \sim 7$ MeV/c^2, therefore the ω mass is not constrained to its nominal value. We define a total width $\sigma_{\rm tot} = \sqrt{\sigma^2 + \Gamma^2/c^4} \simeq 11$ MeV/c^2 and require the ω candidates to satisfy $|m_\omega - \mu_{m_\omega}| < 2.5\sigma_{\rm tot}$ (where μ_{m_ω} is the mean of the ω mass distribution).

4. ρ^0 selection

The ρ^0 mesons originate from $\eta' \to \rho^0\gamma$ and are reconstructed in the $\pi^+\pi^-$ decay mode. The charged tracks must satisfy $p_T(\pi^\pm) > 100$ MeV/c, where p_T is the transverse component of the momentum with respect to the beam axis. We define the helicity angle θ_{ρ^0} as the angle between the direction of the momentum of one of the two pions and that of the η' both evaluated in the ρ^0 center-of-mass frame. Because the ρ^0 is a vector meson, the angular distribution is proportional to $\sin^2\theta_{\rho^0}$ for signal, and is flat for background. The ρ^0 candidates with $|\cos\theta_{\rho^0}| > 0.73$ are rejected. Because of the large ρ^0 natural width $\Gamma = 149.1$ MeV [26], the mass of the ρ^0 candidate must lie within 160 MeV/c^2 around the nominal mass value and no mass constraint is applied.

5. η' selection

The η' mesons are reconstructed in the $\pi^+\pi^-\eta(\to \gamma\gamma)$ and $\rho^0\gamma$ decay modes. These modes account for approximately 46.3% of the total decay rate.

Only the $\eta \to \gamma\gamma$ submode is used in the $\pi^+\pi^-\eta$ reconstruction due to its higher efficiency. The selection is described in Sec. III B 2. For candidates reconstructed in the $\rho^0\gamma$ decay channel we select ρ^0 candidates as described in Sec. III B 4, and the photons must have an energy larger than 200 MeV. As photons coming from π^0 decays may fake signal, a veto as described in Sec. III B 2 is applied. The η' mass resolution is about 3 MeV/c^2 for $\pi^+\pi^-\eta$ and 8 MeV/c^2 for $\rho^0\gamma$.

6. K^0_S selection

The K^0_S mesons are reconstructed through their decay to two charged pions ($\pi^-\pi^+$) which must originate from a common vertex, with a χ^2 probability of the vertex fit that must be larger than 0.1%. We define the flight significance as the ratio L/σ_L, where L is the K^0_S flight length in the plane transverse to the beam axis and σ_L is the resolution on L determined from the vertex fit. The combinatorial background is rejected by requiring a flight significance larger than 5. The reconstructed K^0_S mass resolution is about 2 MeV/c^2 for a core Gaussian part corresponding to about 70% of the candidates and 5 MeV/c^2 for the remaining part, depending on the transverse position of the K^0_S decay within the tracking system (SVT or DCH).

7. D^0 selection

The D^0 mesons are reconstructed in the $K^-\pi^+$, $K^-\pi^+\pi^0$, $K^-\pi^+\pi^-\pi^+$, and $K^0_S\pi^+\pi^-$ decay modes. These modes account for about 29% of the total decay rate. All D^0 candidates must satisfy $p^*(D^0) > 1.1$ GeV/c, where p^* refers to the value of the momentum computed in the $\Upsilon(4S)$ rest frame. That requirement is loose enough so

that various sources of background can populate the sidebands of the signal region.

For the decay modes reconstructed only with tracks, we require that the charged pions originating from the D^0 candidates fulfill $p_T(\pi^\pm) > 400$ MeV/c for $K^-\pi^+$, $p_T(\pi^\pm) > 100$ MeV/c for $K^-\pi^+\pi^-\pi^+$, and $p_T(\pi^\pm) > 120$ MeV/c for $K^0_S\pi^-\pi^+$.

The charged tracks must originate from a common vertex, therefore the χ^2 probability of the vertex fit must be larger than 0.1% for the decay channel $K^-\pi^+$ and larger than 0.5% for the other modes with more abundant background. Because of the increasing level of background present for the various decay modes, the kaon candidates must satisfy from looser to tighter PID criteria for the modes $K^-\pi^+$, $K^-\pi^+\pi^-\pi^+$, and $K^-\pi^+\pi^0$ respectively. For $K^0_S\pi^+\pi^-$, the K^0_S candidates must satisfy the selection criteria described in Sec. III B 6.

For the decay $D^0 \to K^-\pi^+\pi^0$ the combinatorial background can significantly be reduced by using the parametrization of the $K^-\pi^+\pi^0$ Dalitz-plot distribution as provided by the Fermilab E691 experiment [32]. This distribution is dominated by the two K^* resonances ($K^{*0} \to K^-\pi^+$ and $K^{*-} \to K^-\pi^0$) and by the $\rho^+(\pi^+\pi^0)$ resonance. Therefore we select only D^0 candidates that fall in the enhanced region of the Dalitz plot as determined by the above parametrization. The π^0 must satisfy the selections described in Sec. III B 1.

The reconstructed D^0 mass resolution is about 5, 5.5, 6.5, and 11 MeV/c^2 for the decay modes $K^-\pi^+\pi^-\pi^+$, $K^0_S\pi^+\pi^-$, $K^-\pi^+$, and $K^-\pi^+\pi^0$ respectively.

8. D^{*0} selection

The D^{*0} mesons are reconstructed in the $D^0\pi^0$ and $D^0\gamma$ decay modes. The π^0 and D^0 candidates are requested to satisfy the selections described in Sec. III B 1 and III B 7 respectively. The photons from $D^{*0} \to D^0\gamma$ must fulfill the additional condition $E\gamma > 130$ MeV and must pass the π^0 veto as described in Sec. III B 2.

The resolution of the mass difference $\Delta m \equiv m_{D^{*0}} - m_{D^0}$ is about 1.3 MeV/c^2 for $D^0\pi^0$ and 7 MeV/c^2 for $D^0\gamma$.

C. Selection of B-meson candidates

The B candidates are reconstructed by combining a $D^{(*)0}$ with an h^0, with the $D^{(*)0}$ and h^0 masses constrained to their nominal values (except when h^0 is an ω). One needs to discriminate between true B signal candidates and fake B candidates. The fake B candidates originate from combinatorial backgrounds, from other specific B modes, or from the cross-feed events between reconstructed color-suppressed signals.

1. B-mesons kinematic variables

Two kinematic variables are commonly used in *BABAR* to select B candidates: the energy-substituted mass $m_{\rm ES}$ and the energy difference ΔE. These two variables use constraints from the precise knowledge of the beam energies and from energy conservation in the two-body decay $\Upsilon(4S) \to B\bar{B}$. The quantity $m_{\rm ES}$ is the invariant mass of the B candidate where the B energy is set to the beam energy in the CM frame:

$$m_{\rm ES} = \sqrt{\left(\frac{s/2 + \vec{p}_0\cdot\vec{p}_B}{E_0}\right)^2 - |\vec{p}_B|^2}. \quad (1)$$

The variable ΔE is the energy difference between the reconstructed B energy and the beam energy in the CM frame:

$$\Delta E = E^*_{D^{(*)}} + E^*_h - \sqrt{s}/2, \quad (2)$$

where $\sqrt{s}$ is the e^+e^- center-of-mass energy. The small variations of the beam energy over the duration of the run are corrected when calculating $m_{\rm ES}$. For the momentum $\vec{p}_i$ ($i = 0, B$) and the energy E_0, the subscripts 0 and B refer to the e^+e^- system and the reconstructed B meson, respectively. The energies $E^*_{D^{(*)}}$ and E^*_h are calculated from the measured $D^{(*)0}$ and h^0 momenta.

For the various decay channels of the B signal events, the $m_{\rm ES}$ distribution peaks at the B mass with a resolution of 2.6–3 MeV/c^2, dominated by the beam energy spread, whereas ΔE peaks near zero with a resolution of 15–50 MeV depending on the number of photons in the final state.

2. Rejection of $e^+e^- \to q\bar{q}$ background

The continuum background $e^+e^- \to q\bar{q}$, where q is a light quark u, d, s, or c, creates high momentum mesons $D^{(*)0}$, π^0, $\eta^{(\prime)}$, ω that can fake the signal mesons originating from the two-body decays $\bar{B}^0 \to D^{(*)0}h^0$. That background is dominated by $c\bar{c}$ processes and to a lesser extent by $s\bar{s}$ processes. Since the B mesons are produced almost at rest in the $\Upsilon(4S)$ frame, the $\Upsilon(4S) \to B\bar{B}$ event shape is isotropically distributed. By comparison, the $q\bar{q}$ events have a back-to-back jetlike shape. The $q\bar{q}$ background is therefore discriminated by employing event shape variables. The following set of variables was found to be optimal among various tested configurations:

(i) The thrust angle θ_T defined as the angle between the thrust axis of the B candidate and the thrust axis of the rest of event, the thrust axis being the axis on which the sum of projected momentum is maximal. The distribution of $|\cos\theta_T|$ is flat for signal and peaks at 1 for continuum background.

(ii) Event shape monomials L_0 and L_2 defined as

$$L_0 = \sum_i |\vec{p}^*_i|; \qquad L_2 = \sum_i |\vec{p}^*_i|\cos^2\theta^*_i, \quad (3)$$

with $\vec{p}^*_i$ being the CM momentum of the particle i that does not come from the B candidate, and θ^*_i is

the angle between $\vec{p}_i^*$ and the thrust axis of the B candidate.

(iii) The polar angle θ_B^* between the B momentum in the $\Upsilon(4S)$ frame and the beam axis. With the $\Upsilon(4S)$ being vector and the B mesons being pseudoscalar, the angular distribution is proportional to $\sin^2\theta_B^*$ for signal and roughly flat for background.

These four variables are combined into a Fisher discriminant built with the *TMVA* [33] toolkit package. An alternate approach employing a multilayer perceptron artificial neural network with two hidden layers within the same framework was tested and showed marginal relative gain, therefore the Fisher discriminant is used.

The Fisher discriminant $\mathcal{F}_{\rm shape}$ is trained with signal MC events and off-peak data events. In order to maximize the number of off-peak events all the $\bar{B}^0 \to D^{(*)0}h^0$ modes are combined. We retain signal MC events with $m_{\rm ES}$ in the signal region 5.27–5.29 MeV/c^2 and off-peak data events with $m_{\rm ES}$ in the range 5.25–5.27 MeV/c^2, accounting for half of the 40 MeV CM energy-shift below the $\Upsilon(4S)$ resonance. The training and testing of the multivariate classifier are performed with nonoverlapping data samples of equal size obtained from a cocktail of 20 000 MC simulation signal events and from 20 000 off-peak events. The obtained Fisher formula is

$$\mathcal{F}_{\rm shape} = 2.36 - 1.18 \times |\cos\theta_T| + 0.20 \times L_0 - 1.01 \times L_2 - 0.80 \times |\cos\theta_B^*|. \quad (4)$$

The $q\bar{q}$ background is reduced by applying a selection cut on $\mathcal{F}_{\rm shape}$. The selection is optimized for each of the 72 signal decay channels by maximizing the statistical significance with signal MC against generic MC $e^+e^- \to q\bar{q}$, $q \neq b$. This requirement for the various decay modes retains between about 30% and 97% of B signal events, while rejecting between about 98% and 35% of the background from light $q\bar{q}$.

3. Rejection of other specific backgrounds

The ω mesons in $\bar{B}^0 \to D^0\omega$ decays are longitudinally polarized. We define the angle θ_ω [7,34] as the the angle between the normal to the plane of the three daughter pions in the ω frame and the line-of-flight of the $\bar{B}^0$ meson in the ω rest frame. This definition is the equivalent of the two-body helicity angle for the three-body decay. To describe the three-body decay distribution of $\omega \to \pi^+\pi^-\pi^0$, we define the *Dalitz angle* θ_D [7] as the angle between the π^0 momentum in the ω frame and the π^+ momentum in the frame of the pair of charged pions.

The signal distribution is proportional to $\cos^2\theta_\omega$ and $\sin^2\theta_D$, while the combinatorial background distribution is roughly flat as a function of $\cos\theta_\omega$ and $\cos\theta_D$. These two angles are combined into a Fisher discriminant $\mathcal{F}_{\rm hel}$ built from signal MC events and generic $q\bar{q}$ and $B\bar{B}$ MC events:

$$\mathcal{F}_{\rm hel} = -1.41 - 1.01 \times |\cos\theta_D| + 3.03 \times |\cos\theta_\omega|. \quad (5)$$

We require $\bar{B}^0 \to D^0\omega$ candidates to satisfy $\mathcal{F}_{\rm hel} > -0.1$, to obtain an efficiency (rejection) on signal (background) of about 85% (62%).

We also exploit the angular distribution properties in the decay $D^{*0} \to D^0\pi^0$ to reject combinatorial background. We define the helicity angle θ_{D^*} as the angle between the line-of-flight of the D^0 and that of the $\bar{B}^0$, both evaluated in the D^{*0} rest frame. The angular distribution is proportional to $\cos^2\theta_{D^*}$ for signal and roughly flat for combinatorial background. Although in principle such a behavior could be employed for $\bar{B}^0 \to D^{*0}\pi^0$, $D^{*0}\eta$, and $D^{*0}\eta'$, a selection on $|\cos\theta_{D^*}|$ significantly improves the statistical significance for the $\bar{B}^0 \to D^{*0}\pi^0$ mode only. Therefore D^{*0} candidates coming from the decay $\bar{B}^0 \to D^{*0}\pi^0$ are required to satisfy $|\cos\theta_{D^*}| > 0.4$ with an efficiency (rejection) on signal (background) of about 91% (33%).

A major $B\bar{B}$ background contribution in the analysis of the $\bar{B}^0 \to D^{(*)0}\pi^0$ decay channel comes from the color-allowed decay $B^- \to D^{(*)0}\rho^-$. If the charged pion (mostly slow) from the decay $\rho^- \to \pi^-\pi^0$ is omitted in the reconstruction of the $\bar{B}^0$ candidate, $B^- \to D^{(*)0}\rho^-$ events can mimic the $D^{(*)0}\pi^0$ signal. Moreover, the decay modes $\mathcal{B}(B^- \to D^{(*)0}\rho^-)$ are 30–50 times larger than those of the $\bar{B}^0 \to D^{(*)0}\pi^0$ modes, and are poorly known: $\Delta\mathcal{B}/\mathcal{B} =$ 13.4%–17.3% [26]. A veto is applied to reduce this background. For each $\bar{B}^0 \to D^{(*)0}\pi^0$ candidate, we combine any remaining negatively charged track in the event to reconstruct a B^- candidate in the decay mode $D^{(*)0}\rho^-$. If the reconstructed B^- candidate satisfies $m_{\rm ES}(B^-) > 5.27$ GeV/c^2, $|\Delta E(B^-)| < 100$ MeV, and $|m_{\rho^-} - m_{\rho^-}^{\rm PDG}| < 250$ MeV/c^2, then the initial $\bar{B}^0$ candidate is rejected. For the analysis of the decay mode $\bar{B}^0 \to D^0\pi^0$ ($B^- \to D^{*0}\pi^0$), the veto retains about 90% (82%) of signal and rejects about 67% (56%) of $B^- \to D^0\rho^-$ and 44% (66%) of $B^- \to D^{*0}\rho^-$ background.

4. Choice of the "best" B candidate in the event

The average number of $\bar{B}^0 \to D^{(*)0}h^0$ candidates per event after all selections ranges between 1 and 1.6 depending on the complexity of the subdecays. We perform all the 72 $\bar{B}^0 \to D^{(*)0}h^0$ decay mode analyzes in parallel. Such that each possible decay channel is selected with a dedicated analysis, for a given decay mode one B candidate only is kept per event. The chosen B is that with the smallest value of

$$\chi^2_B = \left(\frac{m_{D^0} - \mu_{m_{D^0}}}{\sigma_{m_{D^0}}}\right)^2 + \left(\frac{m_{h^0} - \mu_{m_{h^0}}}{\sigma_{m_{h^0}}}\right)^2, \quad (6)$$

for D^0h^0 modes, and

$$\chi^2_B = \left(\frac{m_{D^0} - \mu_{m_{D^0}}}{\sigma_{m_{D^0}}}\right)^2 + \left(\frac{m_{h^0} - \mu_{m_{h^0}}}{\sigma_{m_{h^0}}}\right)^2 + \left(\frac{\Delta m - \mu_{\Delta m}}{\sigma_{\Delta m}}\right)^2, \tag{7}$$

for the $D^{*0}h^0$ modes. The quantities $\sigma_{m_{D^0}}$ and $\sigma_{m_{h^0}}$ ($\mu_{m_{D^0}}$ and $\mu_{m_{h^0}}$) are the resolution (mean) of the mass distributions. The quantities $\mu_{\Delta m}$ and $\sigma_{\Delta m}$ are, respectively, the mean and resolution of the Δm distributions. These quantities are obtained from fits of the mass distribution of simulated candidates selected from signal MC simulations.

The probability of choosing the true $\bar{B}^0$ candidate in the event according to the above criteria ranges from 71 to 100%. The cases with lower probabilities correspond to the $D^{(*)0}h^0$ modes with high neutral multiplicity.

5. Selection efficiencies

The branching fractions of the $\bar{B}^0 \to D^{(*)0}h^0$ decays is computed as

$$\mathcal{B}(\bar{B}^0 \to D^{(*)0}h^0) = \frac{N_S}{N_{B\bar{B}} \cdot \mathcal{E} \cdot \mathcal{B}_{\rm sec}}, \tag{8}$$

where $\mathcal{B}_{\rm sec}$ is the product of the branching fractions associated with the secondary decays of the $D^{(*)0}$ and h^0 mesons for the each of the 72 decay channels considered in this paper [26]. $N_{B\bar{B}}$ is the number of $B\bar{B}$ pairs in data and N_S is the number of signal events remaining after all the selections. The quantity $\mathcal{E}$ is the total signal efficiency including reconstruction (detector and trigger acceptance) and analysis selections. It is computed from each of the 72 exclusive high statistics MC simulation samples.

The selection efficiency from MC simulation is slightly different from the efficiency in data. The MC efficiency and its systematic uncertainty therefore has to be adjusted according to control samples. For the reconstruction of π^0/γ, the efficiency corrections are obtained from detailed studies performed with a high statistics and high purity control sample of π^0 mesons produced in $\tau \to \rho(\pi\pi^0)\nu_\tau$ decays normalized to $\tau \to \pi\nu_\tau$, to unfold tracking effects. Such corrections are validated against studies performed on the relative ratio of the number of detected D^0 mesons in the decays $D^0 \to K^-\pi^+\pi^0$ and $D^0 \to K^-\pi^+$, and produced in the decay of D^{*+} mesons from $e^+e^- \to c\bar{c}$ events. The relative data/simulation efficiency measurements for charged tracks are similarly based on studies of track misreconstruction using $e^+e^- \to \tau^+\tau^-$ events. On one side the events are tagged from a lepton in the decay $\tau^- \to l^-\bar{\nu}_l\nu_\tau$ and on the other side one reconstructs two or three tracks from the decay $\tau^+ \to \pi^+\pi^-h^+\bar{\nu}_\tau$. The simulated efficiency of charged particle identification is compared to the efficiency computed in data with control samples of kaons from $D^{*+} \to D^0(K^-\pi^+)\pi^+$ produced in $e^+e^- \to c\bar{c}$ events. The efficiency for K^0_S candidates is modified using a data sample of K^0_S, mainly arising from the continuum processes e^+e^- into $q\bar{q}$.

The efficiency corrections for the selection criteria applied to $D^{(*)0}$ candidates and on the Fisher discriminant ($\mathcal{F}_{\rm hel}$) for the continuum $q\bar{q}$ ($q \neq b$) rejection are obtained from studies of a $B^- \to D^{(*)0}\pi^-$ control sample. This abundant control sample is chosen for its kinematic similarity with $\bar{B}^0 \to D^{(*)0}h^0$. The corrections are computed from the ratios $\mathcal{E}_{\rm rel.}({\rm data})/\mathcal{E}_{\rm rel.}({\rm MC})$, where the relative efficiencies $\mathcal{E}_{\rm rel.}$ are computed with the signal yields as obtained from fits to $m_{\rm ES}$ distributions of $B^- \to D^{(*)0}\pi^-$ candidates in data and MC simulation, before and after applying the various selections. The obtained results are checked with the color-allowed control sample $B^- \to D^{(*)0}\rho^-$, which has slightly different kinematics due to the relatively higher mass of the ρ^-, and therefore validates those corrections for the modes such as $D^{(*)0}\eta'$.

The reconstruction efficiency of $\bar{B}^0 \to D^{*0}\omega$ depends on the angular distribution, which is not yet known ($f_L \sim 0.5$–1). To evaluate this efficiency we combine a set of properly weighted fully longitudinally and fully transversely polarized MC samples, according to the fraction of longitudinal polarization that we measure in this paper (see Sec. VI).

D. Fit procedure and data distributions

We present the fits used to extract the branching fractions $\mathcal{B}$. For each of the 72 possible $\bar{B}^0 \to D^{(*)0}h^0$ subdecay modes, using an iterative procedure (discussed in Sec. III D 5), we fit the ΔE distribution in the range $|\Delta E| < 280$ MeV for $m_{\rm ES} > 5.27$ GeV/c^2 to get the signal (N_S) and background yields. The fit of the ΔE distribution allows us to model and adjust the complex noncombinatoric B background structure without relying completely on simulation.

The data samples corresponding to each $\bar{B}^0$ decay mode are disjoint and the fits are performed independently for each mode. According to their physical origin, four categories of events with differently shaped ΔE distributions are considered: signal events, cross-feed events, peaking background events, and combinatorial background events. The event (signal and background) yields are obtained from unbinned extended maximum likelihood (ML) fits. We write the extended likelihood $\mathcal{L}$ as

$$\mathcal{L} = \frac{e^{-n}}{N!} n^N \prod_{j=1}^{N} f(\Delta {\rm E}_j|\theta, n), \tag{9}$$

where θ indicates the set of parameters which are fitted from the data. N is the total number of signal and background events for each subdecay mode, and $n = \sum_i N_i$ is the expectation value for the total number of events. The sum runs over the different expected number N_i of signal and background events in the various i categories. The total probability density function (PDF) $f(\Delta E_j|\theta, n)$ is written as the sum over the different signal and background categories,

$$f(\Delta E_j|\theta, n) = \frac{\sum_i N_i f_i(\Delta E_j|\theta)}{n}, \quad (10)$$

where $f_i(\Delta E|\theta)$ is the PDF of category i (signal or background component). Some of the PDF component parameters are fixed from the MC simulation (see details in the following sections).

The individual corresponding branching ratios are computed and then combined as explained in Sec. V.

1. Signal contribution

All of the 72 possible reconstructed $\bar{B}^0$ decay channels contain at least one photon. Because of the possible energy losses of early showering photons in the detector material before the EMC, the ΔE shape for signal is modeled by the *modified Novosibirsk* PDF [31]. A Gaussian PDF is added to the modes with a large ΔE resolution to describe misreconstructed events. The signal shape parameters are estimated from a ML fit to the distributions of simulated signal events in the high statistics exclusive decay modes.

2. Cross-feed contribution

We call "cross feed" the events from all of the reconstructed $D^{(*)0}h^0$ modes, except the one under consideration, that pass the complete selection. The cross-feed events are a non-negligible part of the ΔE peak in some of the modes, and the signal event yield must be corrected for these cross-feed events. As the various decay channels are studied in parallel, we use an iterative procedure to account for those contributions in the synchronous measurements (see Sec. III D 5).

The dominant cross-feed contribution to $\bar{B}^0 \to D^0 h^0$ comes from the companion decay channel $\bar{B}^0 \to D^{*0}h^0$, when the π^0/γ from the D^{*0} decay is not reconstructed. Such cross-feed events are shifted in ΔE by approximately the mass of the π^0 (-135 MeV), with a long tail from $D^{*0}(\to D^0\gamma)h^0$ leaking into the signal region. Similarly, the decay channel $\bar{B}^0 \to D^{*0}h^0$ receives a cross-feed contribution from the associated decay mode $\bar{B}^0 \to D^0 h^0$ and there is a cross-contamination between the $D^{*0} \to D^0\pi^0$ and $D^{*0} \to D^0\gamma$ decay channels.

The remaining cross-feed contributions, *i.e.* from other $\bar{B}^0 \to D^{(*)0}h^0$ color-suppressed decay modes, were studied with the generic MC simulation. They were found to be highly negligible and represent at most 1% of the signal, in the region $|\Delta E| < 100$ MeV. Therefore they are accounted for by the generic MC simulation, whose generated branching fractions were taken from the PDG [26].

3. Peaking $B\bar{B}$ background contributions

The major background in the reconstruction of $\bar{B}^0 \to D^{(*)0}\pi^0$ comes from the decays $B^- \to D^{(*)0}\rho^-$ (see Sec. III C 3). Their contribution is modeled by histogram-based PDFs built from the high statistics exclusive signal MC simulation samples. The individual distributions of the two backgrounds $B^- \to D^0\rho^-$ and $B^- \to D^{*0}\rho^-$ that pass the $\bar{B}^0 \to D^{(*)0}\pi^0$ selections, including the specific veto requirement as described in Sec. III C 3, cannot be distinguished. As a consequence, given the large uncertainty on their branching fractions, the overall normalization of $B^- \to D^{(*)0}\rho^-$ PDF is left floating but the relative ratio $N(B^- \to D^{*0}\rho^-)/N(B^- \to D^0\rho^-)$ of the PDF normalization is fixed. The value of this ratio is extracted directly from the data by reconstructing exclusively each of the $B^- \to D^{(*)0}\rho^-$ modes rejected by the veto requirements. Those fully reconstructed B^- mesons differ from the $B^- \to D^{(*)0}\rho^-$, that pass all the $\bar{B}^0 \to D^{(*)0}\pi^0$ selections, by the additional selected slow charged π originated from the ρ^- meson. The relative correction on that ratio for events surviving the veto selection is then computed using the MC simulation for generated $B^- \to D^{(*)0}\rho^-$ decays. A systematic uncertainty on that assumption is assigned (see Sec. IV).

In the cases of $\bar{B}^0 \to D^{(*)0}\omega/\eta(\to \pi^+\pi^-\pi^0)$ modes, additional contributions come from the B decay modes $D^{(*)}n\pi\pi^{(0)}$, where $n = 1$, 2, or 3, and through intermediate resonances such as ω and $\rho_3^-(1690)(\to \omega\pi^-)$. These peaking backgrounds are modeled by a first-order polynomial PDF plus a Gaussian PDF determined from the generic $B\bar{B}$ MC simulation. The relative normalization of that Gaussian PDF component is left floating in the fit, since some of the branching fractions of the B decay modes $D^{(*)}n\pi\pi^{(0)}$ are not precisely known [26].

4. Combinatorial background contribution

The shape parameters of the combinatorial background PDFs are obtained from ML fits to the generic $B\bar{B}$ and continuum MC, where all signal, cross feed and peaking $B\bar{B}$ background events have been removed. The combinatorial background from $B\bar{B}$ and $q\bar{q}$ ($q \neq b$) are summed and modeled by a second-order polynomial PDF.

5. Iterative fitting procedure

We fit the ΔE distribution using the PDFs for the signal, for the cross feed, for the peaking background, and for the combinatorial background as detailed in the previous sections. The normalization of the signal, the peaking $B\bar{B}$ backgrounds, and the combinatorial background components are allowed to float in the fit. The mean of the signal PDF is left floating for the sum of $D^{(*)0}$ subdecays. For each D^0 submode, the signal mean PDF is fixed to the value obtained from the fit to the sum of D^0 submodes. Those free parameters are extracted by maximizing the unbinned extended likelihood to the ΔE distribution defined in Eqs. (9) and (10). Other PDF parameters are fixed from fit results obtained with MC simulations, when studying separately each of the signal and background categories.

In the global event yield extraction of all the various $\bar{B}^0 \to D^{(*)0}h^0$ color-suppressed signals studied in this paper, a given mode can be signal and cross feed to other

modes at the same time. In order to use the $\mathcal{B}$ computed in this analysis, the yield extraction is performed through an iterative fit on $D^{*0}h^0$ and D^0h^0. The normalization of cross-feed contribution from $D^{(*)0}h^0$ is then fixed to the $\mathcal{B}$ measured in the previous fit iteration. For the cross-feed contributions, the PDG branching fraction [26] values are used as starting points. This iterative method converges quickly to stable $\mathcal{B}$ values, with a variation of less than 10% of the statistical uncertainty, in less than 5 iterations.

We check the absence of biases in our fit procedure by studying pseudoexperiments with a large number of different data-sized samples for the various signals. The extraction procedure is applied to these samples where background events are generated and added from the fitted PDFs. The signal samples are assembled from nonoverlapping samples corresponding to the exclusive high statistics MC signals, with yields corresponding to the MC-generated value of the branching fraction. No significant biases are found.

6. Data distributions and event yields from summed subdecay modes

The fitting procedure is applied to data at the very last stage of the blind analysis. Though the event yields and $\mathcal{B}$ measurements are performed separately for each of the 72 considered subdecay modes, we illustrate here, in a compact manner, the magnitude of the signal and background component yields, and the statistical significances, of the various decay channels $\bar{B}^0 \to D^{(*)0}h^0$, summing together all the D^0 submodes. The fitted ΔE distributions, for the sum of D^0 submodes, are given in Figs. 2–4, for, respectively, the $\bar{B}^0 \to D^0h^0$, $D^{*0}(\to D^0\pi^0)h^0$, and $D^{*0}(\to D^0\gamma)h^0$ modes.

The signal and background yields obtained from the fit to the summed submode data for the $\bar{B}^0 \to D^{(*)0}h^0$ are presented in Table I, with the corresponding statistical significances. The signal and background yields are computed in the signal region $|\Delta E| < 2.5\sigma$ (where σ is the signal resolution). In the same range we calculate the statistical significance of the various signals from the cumulative Poisson probability p to have a background statistical fluctuation reaching the observed data yield,

$$p = \sum_{k=N_{\rm cand}}^{+\infty} \frac{e^{-\nu}}{k!}\nu^k, \tag{11}$$

where $N_{\rm cand}$ is the total number of selected candidates in the signal region and ν the mean value of the total expected background, as extracted from the fit. This probability is then converted into a number of equivalent one-sided standard deviations $\mathcal{S}_{\rm stat}$,

$$\mathcal{S}_{\rm stat} = \sqrt{2}\,\texttt{erfcInverse}(p/2). \tag{12}$$

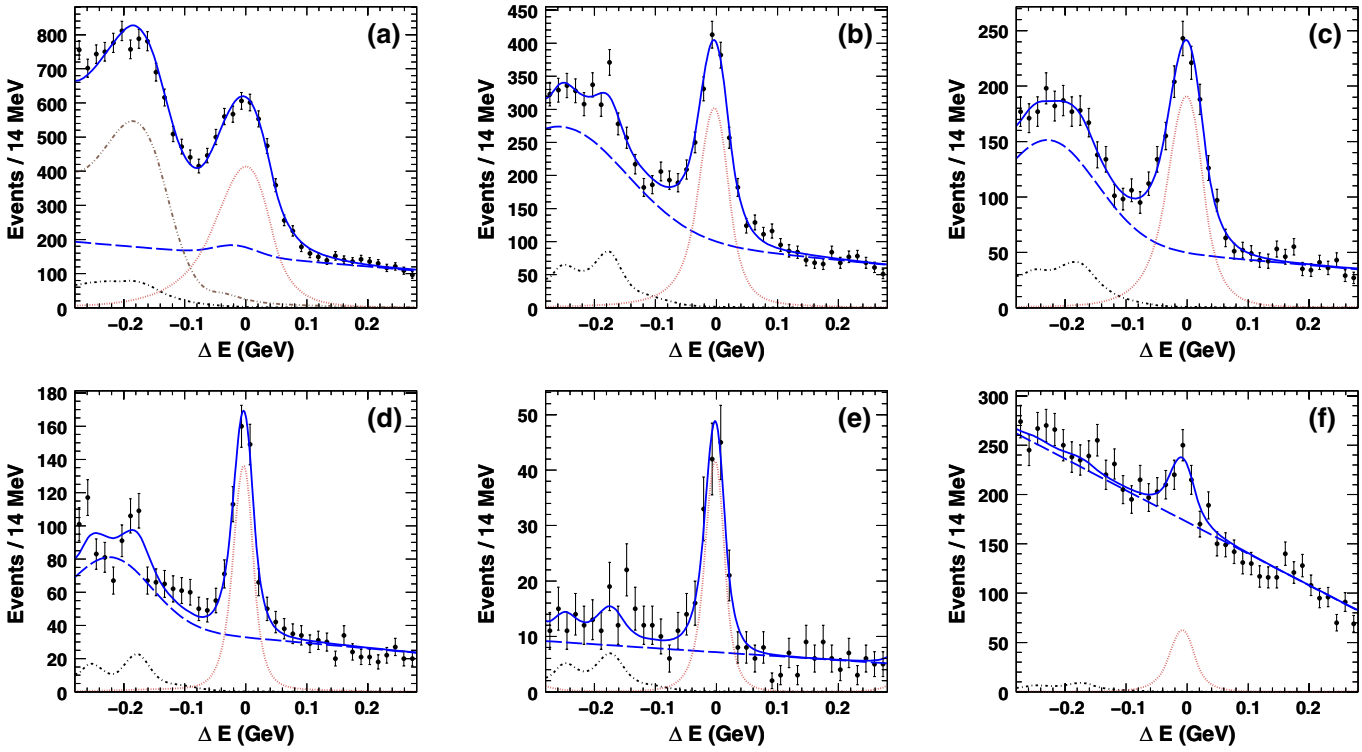

FIG. 2 (color online). Fits of ΔE distributions in data for modes $\bar{B}^0 \to D^0\pi^0$ (a), $\bar{B}^0 \to D^0\omega$ (b), $\bar{B}^0 \to D^0\eta(\gamma\gamma)$ (c), $\bar{B}^0 \to D^0\eta(\pi\pi\pi^0)$ (d), $\bar{B}^0 \to D^0\eta'(\pi\pi\eta)$ (e), and $\bar{B}^0 \to D^0\eta'(\rho^0\gamma)$ (f). The data points with error bars are measurements in data, the curves are the various PDF components: the solid (blue) fitted total PDF, the dotted (red) signal PDF, the dotted-dashed (black) cross-feed PDF, the double dotted-dashed (brown) $B^- \to D^{(*)0}\rho^-$ PDF, and the long dashed (blue) combinatorial background PDF.

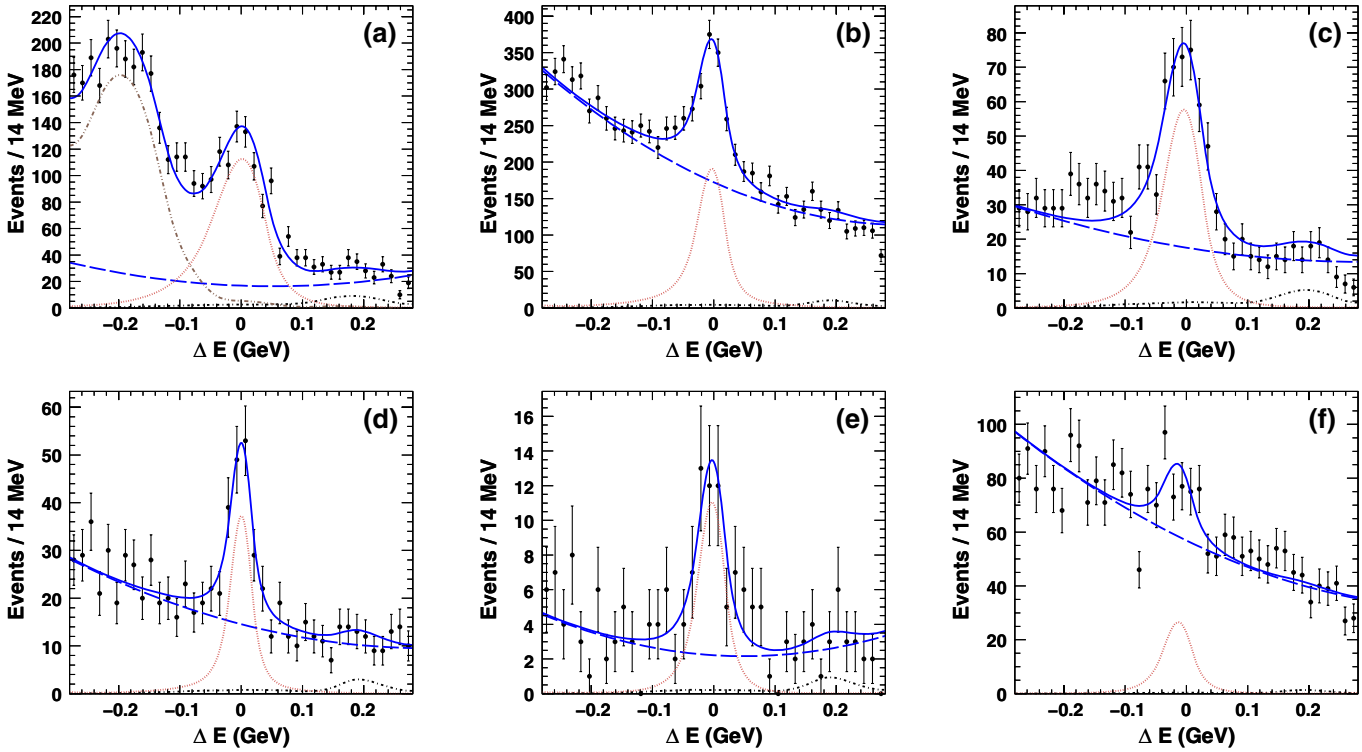

FIG. 3 (color online). Fits of ΔE distributions in data for modes $\bar{B}^0 \to D^{*0}\pi^0$ (a), $\bar{B}^0 \to D^{*0}\omega$ (b), $\bar{B}^0 \to D^{*0}\eta(\gamma\gamma)$ (c), $\bar{B}^0 \to D^{*0}\eta(\pi\pi\pi^0)$ (d), $\bar{B}^0 \to D^{*0}\eta'(\pi\pi\eta)$ (e), and $\bar{B}^0 \to D^{*0}\eta'(\rho^0\gamma)$ (f), where the D^{*0} mesons decay into the signal mode $D^0\pi^0$. A detailed legend is provided in the caption of Fig. 2.

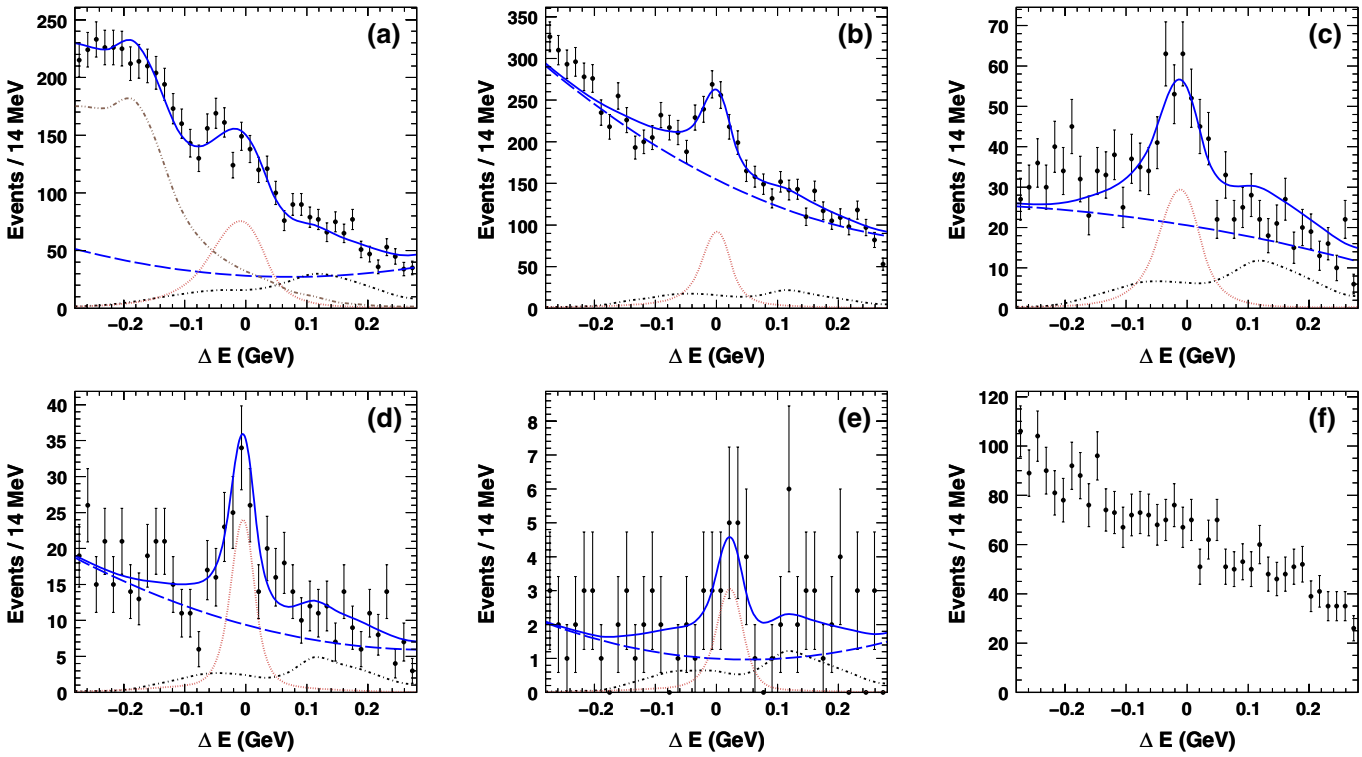

FIG. 4 (color online). Fits of ΔE distributions in data for modes $\bar{B}^0 \to D^{*0}\pi^0$ (a), $\bar{B}^0 \to D^{*0}\omega$ (b), $\bar{B}^0 \to D^{*0}\eta(\gamma\gamma)$ (c), $\bar{B}^0 \to D^{*0}\eta(\pi\pi\pi^0)$ (d), and $\bar{B}^0 \to D^{*0}\eta'(\pi\pi\eta)$ (e), where the D^{*0} mesons decay into the signal mode $D^0\gamma$. The unfitted ΔE distribution of $\bar{B}^0 \to D^{*0}(D^0\gamma)\eta'(\rho^0\gamma)$ candidates is also displayed (f). A detailed legend is provided in the caption of Fig. 2.

TABLE I. Numbers of signal events (N_S), combinatorial background ($N_{\rm combi}$), cross feed ($N_{\rm cf}$), and $B^- \to D^{(*)0}\rho^-$ ($N_{D\rho}$) events computed from the ΔE fits to data and counted in a signal box $|\Delta E| < 2.5\sigma$, together with the statistical significances in numbers of standard deviations $\mathcal{S}_{\rm stat}$ (see text). The quoted uncertainties are statistical only.

$\bar{B}^0 \to$ (decay channel)	N_S	$N_{\rm combi}$	$N_{\rm cf}$	$N_{D\rho}$	Statistical significance $\mathcal{S}_{\rm stat}$
$D^0\pi^0$	3429 ± 123	2625 ± 75	97 ± 3	700 ± 14	41
$D^0\eta(\gamma\gamma)$	1022 ± 55	532 ± 14	13 ± 1	-	36
$D^0\eta(\pi\pi\pi^0)$	411 ± 29	191 ± 6	2 ± 0	-	23
$D^0\omega$	1374 ± 120	886 ± 25	18 ± 2	-	38
$D^0\eta'(\pi\pi\eta(\gamma\gamma))$	122 ± 13	41 ± 3	-	-	14
$D^0\eta'(\rho^0\gamma)$	234 ± 40	1253 ± 17	1 ± 0	-	7.4
$D^{*0}(D^0\pi^0)\pi^0$	883 ± 40	268 ± 21	39 ± 2	175 ± 5	34
$D^{*0}(D^0\gamma)\pi^0$	622 ± 47	469 ± 33	295 ± 23	602 ± 20	17
$D^{*0}(D^0\pi^0)\eta(\gamma\gamma)$	338 ± 25	201 ± 9	17 ± 1	-	19
$D^{*0}(D^0\gamma)\eta(\gamma\gamma)$	187 ± 24	254 ± 12	85 ± 11	-	8.7
$D^{*0}(D^0\pi^0)\eta(\pi\pi\pi^0)$	123 ± 15	90 ± 4	5 ± 1	-	11
$D^{*0}(D^0\gamma)\eta(\pi\pi\pi^0)$	88 ± 14	65 ± 4	16 ± 3	-	7.6
$D^{*0}(D^0\pi^0)\omega$	806 ± 48	1365 ± 18	33 ± 2	-	20
$D^{*0}(D^0\gamma)\omega$	414 ± 44	1290 ± 19	132 ± 14	-	10
$D^{*0}(D^0\pi^0)\eta'(\pi\pi\eta)$	45 ± 8	18 ± 2	2 ± 0	-	8.5
$D^{*0}(D^0\gamma)\eta'(\pi\pi\eta)$	12 ± 5	8 ± 1	5 ± 2	-	3.2
$D^{*0}(D^0\pi^0)\eta'(\rho^0\gamma)$	115 ± 25	487 ± 11	3 ± 1	-	5.4

The function `erfcInverse` is the inverse of the complementary error function (see statistics review in [26]).

The majority of the decay channels present clear and significant signals. In particular, the modes $D^0\eta'(\pi\pi\eta(\gamma\gamma))$ and $D^0\eta'(\rho^0\gamma)$ are observed for the first time.

Before performing the final unblinded fits on data, among the various 72 initial possible decay channels, several subdecay modes have been discarded. The decision to remove those submodes have been taken according to analyses performed on MC simulation, as no significant signals are expected. The eliminated decay channels are: $\bar{B}^0 \to D^{(*)0}\eta'$ and $D^{*0}(D^0\gamma)\eta(\pi\pi\pi^0)$, where $D^0 \to K^0_S\pi^+\pi^-$, $D^{*0}(D^0\gamma)\eta'(\pi\pi\eta)$, where $D^0 \to K^-\pi^+\pi^-\pi^+$, as well as the whole decay channel $D^{*0}(D^0\gamma)\eta'(\rho^0\gamma)$. These are submodes with poor signal efficiency, caused by large track multiplicity or modest D^0 secondary branching fractions, such that the expected signal yields are very low. In addition, they have large background contributions. We concluded that adding such decay channels in the global combinations would degrade the $\mathcal{B}$ measurements. These choices based on a Monte Carlo simulation only studies have been confirmed in data (see, for example, Fig. 4 (bottom right)).

IV. SYSTEMATIC UNCERTAINTIES ON BRANCHING FRACTIONS

There are several possible sources of systematic uncertainties in this analysis, which are summarized in Table II.

TABLE II. Combined contributions to the branching fraction $\mathcal{B}(\bar{B}^0 \to D^{(*)0}h^0)$ relative systematic uncertainties (%).

Sources	$\Delta\mathcal{B}/\mathcal{B}$(%) for the $\bar{B}^0$ decay									
	$D^0\pi^0$	$D^0\eta(\gamma\gamma)$	$D^0\eta(\pi\pi\pi^0)$	$D^0\omega$	$D^0\eta'(\pi\pi\eta)$	$D^0\eta'(\rho^0\gamma)$	$D^{*0}\pi^0$	$D^{*0}\eta$	$D^{*0}\omega$	$D^{*0}\eta'$
π^0/γ detection	3.5	3.5	3.6	3.6	3.7	2.3	6.2	5.5	5.7	5.8
Tracking	0.9	0.9	1.6	1.7	1.6	1.6	0.9	1.1	1.6	1.6
Kaon ID	1.0	1.1	1.1	1.1	1.2	1.1	1.1	1.1	1.1	1.2
K^0_S reconstruction	0.7	0.7	0.6	0.8	0.6	0.6	0.4	0.3	0.5	-
Secondary $\mathcal{B}$	1.6	1.6	2.0	1.8	2.3	2.4	5.1	5.7	5.5	5.1
$B\bar{B}$ counting	1.1	1.1	1.1	1.1	1.1	1.1	1.1	1.1	1.1	1.1
MC statistics	0.1	0.2	0.3	0.2	0.4	0.4	0.2	0.2	0.3	0.3
Particles selection	0.3	0.4	0.2	1.0	0.3	1.0	0.2	0.1	0.1	1.2
ΔE fit	2.1	2.2	1.3	2.1	1.1	2.1	1.0	0.6	1.4	0.5
Combinatorial background	0.1	0.1	0.1	0.1	0.1	0.1	0.1	0.1	0.1	0.1
$D^{(*)0}\rho^-$ background	1.8	-	-	-	-	-	5.6	-	-	-
$D^{*0}\omega$ polarization	-	-	-	-	-	-	-	-	1.4	-
Total	5.1	4.9	4.9	5.3	5.1	4.7	9.6	8.2	8.5	8.2

The categories "π^0/γ detection" and "Tracking" account, respectively, for the systematic uncertainties on the reconstruction of π^0/γ and for charged particle tracks, and are taken from the efficiency corrections computed in the studies of τ decays from $e^+e^- \to \tau^+\tau^-$ events (see Sec. III C 5).

Similarly, the systematic uncertainties on kaon identification and on the reconstruction of K^0_S mesons are estimated from the MC efficiency corrections computed in the study of pure samples of kaons and K^0_S mesons compared to data (see Sec. III C 5).

The uncertainty on the secondary branching fraction results from our limited knowledge of the $D^{(*)0}$ and h^0 submode branching ratios [26] (including secondary decays into detected stable particles). Correlations between the different decay channels were accounted for.

The uncertainty related to the number of $B\bar{B}$ pairs and the limited available MC-sample statistics when computing the efficiency of various selection criteria are also included.

Systematic uncertainties due to the intermediate particles mass selections are computed as the relative difference of signal yield when the values of the mass means and mass resolutions are taken from a fit to the data. Systematic effects from the $q\bar{q}$ ($q \neq b$) rejection and the $D^{(*)0}$ selections are obtained from the study performed on the control sample $B^- \to D^{(*)0}\pi^-$ and are estimated as the limited confidence on the efficiency correction ratio: $\mathcal{E}_{\text{rel.}}(\text{data})/\mathcal{E}_{\text{rel.}}(\text{MC})$, including the correlations between the samples before and after selections (see Sec. III C 5). The effects of the cuts on ρ^0 and $D^0\omega$ helicities are obtained by varying the selection cut values by $\pm 10\%$ around the maximum of statistical significance. All uncertainties on intermediate particle selections are combined into the category "Particles selection".

The uncertainty quoted for "ΔE Fit" gathers the changes due the limited knowledge on the shapes of signal and background PDFs, and on the cross-feed branching fraction. For example, the modes $D^{(*)0}\pi^0/\eta(\gamma\gamma)$ have high or low momentum γ in the final state. The difference between data and MC simulation in energy scale and resolution for neutrals is estimated from a study of the high statistics control sample $B^- \to D^0(K^-\pi^+)\rho^-(\pi^0\pi^-)$, which yields the difference between data and MC simulation, $\simeq 5.7$ MeV, for the mean and $\simeq 3.3$ MeV, for the resolution. This study was cross-checked against another one performed with the high statistics and very pure control sample $B^- \to D^0(K^-\pi^+\pi^0)\pi^-$. With that control sample we find a difference between data and MC simulation of respectively $\simeq 1.7$ MeV, for the mean and $\simeq 0.04$ MeV, for the resolution. For the modes $\bar{B}^0 \to D^{(*)0}\pi^0/\eta(\gamma\gamma)$, the uncertainty due to the signal shape is obtained by varying conservatively the signal PDF mean by ± 5.7 MeV and the width by ± 3.3 MeV. For the other $\bar{B}^0$ signal modes, each PDF parameter is varied within $\pm 1\sigma$ of its MC simulation precision, and the relative difference on the fitted event yield is taken as a systematic incertitude. The various parameters are varied one at a time, independently. The relative differences while varying the ΔE PDF parameters are then summed up in quadrature. This sum is taken as the systematic doubt on the ΔE shapes.

The uncertainty on the combinatorial background shape (including both $B\bar{B}$ and $q\bar{q}$ ($q \neq b$) events) is evaluated from the comparison of generic MC simulation and data in the m_{ES} sidebands: $5.24 < m_{\text{ES}} < 5.26$ GeV$/c^2$. The observed difference between data and simulation has then been used as a systematics. When a Gaussian is added to the combinatorial background shape, to model additional peaking $B\bar{B}$ background contributions (see Sec. III D 3), the related effect is computed by varying its means and resolution by $\pm 1\sigma$.

We account for possible differences in the PDF shape of the $B^- \to D^{(*)0}\rho^-$ background that is modeled by a nonparametric PDF. As above, it is obtained by shifting and smearing the PDF mean and resolution by ± 5.7 MeV and ± 3.3 MeV respectively. The nonparametric PDF is convoluted with a Gaussian with the previously defined mean and width values. The quadratic sum of the various changes on the signal event yield is taken as the systematic uncertainty.

The relative ratio of the $B^- \to D^{*0}\rho^-$ and $B^- \to D^0\rho^-$ backgrounds for the studies of the modes $\bar{B}^0 \to D^{(*)0}\pi^0$ has been fixed to the selected $B^- \to D^{(*)0}\rho^-$ events of the data control sample, for rejected B^- events with the veto described in Sec. III C 3. The effect of such a veto on that ratio is then computed from MC simulation. We assign as a conservative systematic uncertainty half of the difference between the nominal result and the result from the MC simulation assuming the PDG branching ratios of $B^- \to D^{(*)0}\rho^-$ [26].

The acceptance of $\bar{B}^0 \to D^{*0}\omega$ is computed from the sum of purely longitudinally ($f_L = 0$) and transversely ($f_L = 1$) polarized MC simulation signals, weighted by our measurement of f_L (see Sec. VI). The systematic limited knowledge of the efficiency due to the unknown fraction of $D^{*0}\omega$ longitudinal polarization is then estimated by varying f_L by $\pm 1\sigma$ in the estimation of the signal acceptance. This contribution is slightly larger than 1%, while it is expected to be about 10.5% if the fraction f_L were unknown. This is one of the motivations for measuring the polarization of the decay channel $\bar{B}^0 \to D^{*0}\omega$ (see Sec. VI).

The most significant sources of systematic uncertainties come from the π^0/γ reconstruction, the ΔE fits, and the uncertainties on the world average branching fractions of the secondary decay channels. In the case of the modes $\bar{B}^0 \to D^{(*)0}\pi^0$, the contributions from $B^- \to D^{(*)0}\rho^-$ backgrounds are also not negligible.

V. RESULTS FOR THE $\mathcal{B}$ MEASUREMENTS

The branching fractions measured in the different secondary decay channels reconstructed in this analysis are

TABLE III. Branching fractions of the decay channels $\bar{B}^0 \to D^{(*)0}h^0$ measured in the different secondary decay modes. The first uncertainty is statistical and the second is systematic. The cells with "-" correspond to decay channels that have been discarded after the analysis on simulation, and confirmed with data, as no significant signal is expected or seen for them.

$\mathcal{B}(\bar{B}^0 \to)(\times 10^{-4})$	$D^0 \to K\pi$	$D^0 \to K3\pi$	$D^0 \to K\pi\pi^0$	$D^0 \to K^0_S\pi^+\pi^-$
$D^0\pi^0$	$2.49 \pm 0.13 \pm 0.16$	$2.69 \pm 0.15 \pm 0.17$	$2.97 \pm 0.15 \pm 0.25$	$2.90 \pm 0.28 \pm 0.23$
$D^0\eta(\gamma\gamma)$	$2.46 \pm 0.18 \pm 0.14$	$2.56 \pm 0.19 \pm 0.16$	$2.37 \pm 0.20 \pm 0.20$	$2.62 \pm 0.37 \pm 0.21$
$D^0\eta(\pi\pi\pi^0)$	$2.59 \pm 0.27 \pm 0.12$	$2.65 \pm 0.30 \pm 0.14$	$2.48 \pm 0.29 \pm 0.20$	$2.28 \pm 0.54 \pm 0.18$
$D^0\omega$	$2.59 \pm 0.18 \pm 0.20$	$2.34 \pm 0.19 \pm 0.15$	$2.42 \pm 0.20 \pm 0.21$	$3.17 \pm 0.39 \pm 0.24$
$D^0\eta'(\pi\pi\eta(\gamma\gamma))$	$1.40 \pm 0.25 \pm 0.07$	$1.37 \pm 0.26 \pm 0.08$	$1.34 \pm 0.27 \pm 0.11$	$1.30 \pm 0.50 \pm 0.12$
$D^0\eta'(\rho^0\gamma)$	$1.58 \pm 0.42 \pm 0.09$	$1.79 \pm 0.57 \pm 0.10$	$1.91 \pm 0.54 \pm 0.15$	$1.55 \pm 0.89 \pm 0.16$
$D^{*0}(D^0\pi^0)\pi^0$	$2.95 \pm 0.25 \pm 0.30$	$2.95 \pm 0.29 \pm 0.33$	$3.52 \pm 0.29 \pm 0.43$	$2.32 \pm 0.56 \pm 0.24$
$D^{*0}(D^0\gamma)\pi^0$	$3.49 \pm 0.40 \pm 0.83$	$2.25 \pm 0.50 \pm 0.63$	$3.02 \pm 0.50 \pm 0.90$	$3.53 \pm 1.14 \pm 0.99$
$D^{*0}(D^0\pi^0)\eta(\gamma\gamma)$	$2.52 \pm 0.32 \pm 0.26$	$2.57 \pm 0.33 \pm 0.29$	$2.41 \pm 0.32 \pm 0.32$	$4.09 \pm 0.74 \pm 0.49$
$D^{*0}(D^0\gamma)\eta(\gamma\gamma)$	$2.62 \pm 0.45 \pm 0.33$	$2.81 \pm 0.49 \pm 0.35$	$2.87 \pm 0.55 \pm 0.39$	$2.75 \pm 0.78 \pm 0.36$
$D^{*0}(D^0\pi^0)\eta(\pi\pi\pi^0)$	$2.27 \pm 0.50 \pm 0.20$	$2.60 \pm 0.55 \pm 0.24$	$1.93 \pm 0.46 \pm 0.22$	$1.21 \pm 0.87 \pm 0.13$
$D^{*0}(D^0\gamma)\eta(\pi\pi\pi^0)$	$2.93 \pm 0.71 \pm 0.32$	$2.55 \pm 0.80 \pm 0.29$	$1.94 \pm 0.81 \pm 0.24$	-
$D^{*0}(D^0\pi^0)\omega$	$5.07 \pm 0.45 \pm 0.47$	$4.00 \pm 0.49 \pm 0.36$	$4.38 \pm 0.51 \pm 0.51$	$5.02 \pm 0.98 \pm 0.53$
$D^{*0}(D^0\gamma)\omega$	$3.66 \pm 0.64 \pm 0.41$	$4.46 \pm 0.80 \pm 0.56$	$4.59 \pm 0.87 \pm 0.57$	$4.28 \pm 1.71 \pm 0.57$
$D^{*0}(D^0\pi^0)\eta'(\pi\pi\eta(\gamma\gamma))$	$1.09 \pm 0.38 \pm 0.09$	$1.67 \pm 0.44 \pm 0.15$	$1.34 \pm 0.49 \pm 0.15$	-
$D^{*0}(D^0\gamma)\eta'(\pi\pi\eta(\gamma\gamma))$	$0.75 \pm 0.49 \pm 0.24$	-	$1.19 \pm 0.69 \pm 0.39$	-
$D^{*0}(D^0\pi^0)\eta'(\rho^0\gamma)$	$2.10 \pm 0.82 \pm 0.23$	$1.21 \pm 0.90 \pm 0.14$	$1.45 \pm 0.95 \pm 0.18$	-
$D^{*0}(D^0\gamma)\eta'(\rho^0\gamma)$	-	-	-	-

given in Table III (for missing entries in the Table; see the discussion on discarded submodes in Sec. III D 6).

These branching fractions are combined using the so-called Best Linear Unbiased Estimate (*BLUE*) technique [35], that accounts for the correlation between the various modes. In the *BLUE* method the average value is a linear combination of the individual measurements,

$$\mathcal{B} = \sum_{i=1}^{t} (\alpha_i \cdot \mathcal{B}_i), \tag{13}$$

where each coefficient α_i is a constant weight, not necessarily positive, for a given measurement $\mathcal{B}_i$. The condition $\sum_{i=1}^{t} \alpha_i = 1$ ensures that the method is unbiased. The set of coefficients $\alpha = (\alpha_1, \alpha_2, \ldots, \alpha_t)$ is calculated so that the variance of branching fraction is minimal,

$$\alpha = \frac{E^{-1}U}{U^T E^{-1} U}, \tag{14}$$

where U is a t-component vector whose elements are all 1 (U^T is its transpose) and E is the $(t \times t)$ covariance matrix. The variance of branching fraction is then given by

$$\sigma^2 = \alpha^T E \alpha. \tag{15}$$

The covariance matrix E is evaluated for each source of systematics. Its matrix elements are, for two modes i and j,

$$E_{ij} = \rho_{ij}\sigma_i\sigma_j, \tag{16}$$

where σ_i and σ_j are the systematic uncertainties for the modes i and j, and ρ_{ij} is their correlation coefficient. We distinguish several types of systematic uncertainties according to their correlations between the modes:

(i) full correlation, $|\rho_{ij}| \sim 1$: neutrals (but uncertainties for π^0 and single γ are independent), PID, tracking, number of $B\bar{B}$, $\mathcal{B}(D^{*0})$, $D^{*0}\omega$ polarization in that mode,

(ii) medium correlation: $\mathcal{B}(D^0)$, $\mathcal{B}(h^0)$, whose correlations are taken from the PDG [26] and range from 2% to 100%, $D^{(*)0}\rho^-$ background in $\bar{B}^0 \to D^{(*)0}\pi^0$,

(iii) negligible correlation, $|\rho_{ij}| \sim 0$: statistical uncertainties, PDF systematics, selection of intermediate particles, MC statistics.

The total covariance matrix E is then the sum of the covariance matrices for each source of uncertainty, plus the covariance matrix associated to statistical uncertainties. The systematic (statistical) uncertainty on the combined value of branching fraction computed by using Eq. (15) where the error matrix includes only the systematic (statistical) uncertainties.

The combined branching fractions in data are given in Table IV with the χ^2 of the combination, the number of degrees of freedom of the combination (ndof), and the corresponding probability (p-value). The individual branching fractions together with the combined value are displayed in Figs. 5 and 6 and they are compared to the previous measurements by CLEO [10], *BABAR* [7,14], and Belle [11,12].

The results of this analysis, based on a data sample of $454 \times 10^6 B\bar{B}$ pairs, are fully compatible with our previous measurements [7,14], and also with those of CLEO [10]. They are compatible with the measurements by Belle

TABLE IV. Branching fractions of decay channels $\bar{B}^0 \to D^{(*)0}h^0$, where the branching fraction measured in each D^0 modes are combined. For the modes with $h^0 = \eta$, η', we give the combination (comb.) of the branching fraction computed with each submodes of $\eta^{(\prime)}$. The first uncertainty is statistical and the second is systematics. The quality of the combination is given through the value of χ^2/ndof, with the corresponding probability (p-value) given in parenthesis in percents.

$\bar{B}^0$ mode	$\mathcal{B}(\times 10^{-4})$	χ^2/ndof (p-value %)
$D^0\pi^0$	$2.69 \pm 0.09 \pm 0.13$	2.81/3 (42.2)
$D^0\eta(\gamma\gamma)$	$2.50 \pm 0.11 \pm 0.12$	0.45/3 (93.0)
$D^0\eta(\pi\pi\pi^0)$	$2.56 \pm 0.16 \pm 0.13$	0.39/3 (94.2)
$D^0\eta$ (comb.)	$2.53 \pm 0.09 \pm 0.11$	0.95/7 (99.6)
$D^0\omega$	$2.57 \pm 0.11 \pm 0.14$	3.19/3 (36.3)
$D^0\eta'(\pi\pi\eta(\gamma\gamma))$	$1.37 \pm 0.14 \pm 0.07$	0.05/3 (99.7)
$D^0\eta'(\rho^0\gamma)$	$1.73 \pm 0.28 \pm 0.08$	0.27/3 (96.6)
$D^0\eta'$ (comb.)	$1.48 \pm 0.13 \pm 0.07$	1.55/7 (98.1)
$D^{*0}\pi^0$	$3.05 \pm 0.14 \pm 0.28$	4.73/7 (69.3)
$D^{*0}\eta(\gamma\gamma)$	$2.77 \pm 0.16 \pm 0.25$	4.20/7 (75.6)
$D^{*0}\eta(\pi\pi\pi^0)$	$2.40 \pm 0.25 \pm 0.21$	3.81/6 (70.2)
$D^{*0}\eta$ (comb.)	$2.69 \pm 0.14 \pm 0.23$	10.48/14 (72.6)
$D^{*0}\omega$	$4.55 \pm 0.24 \pm 0.39$	4.05/7 (77.4)
$D^{*0}\eta'(\pi\pi\eta(\gamma\gamma))$	$1.37 \pm 0.23 \pm 0.13$	2.30/4 (68.1)
$D^{*0}(D^0\pi^0)\eta'(\rho^0\gamma)$	$1.81 \pm 0.42 \pm 0.16$	0.68/2 (71.2)
$D^{*0}\eta'$ (comb.)	$1.48 \pm 0.22 \pm 0.13$	3.78/7 (80.5)

[11,12] for most of the modes, except for $\bar{B}^0 \to D^{(*)0}\eta$, $D^{*0}\omega$, and $D^{*0}\pi^0$, where our results are larger. Those four branching fractions are from 2.5 to 3.7 standard deviations (including systematic uncertainties) away from the latest measurements by Belle [11,12]. Our measurements are the most precise determinations of the $\mathcal{B}(\bar{B}^0 \to D^{(*)0}h^0)$ from a single experiment. They represent significant improvements with respect to the accuracy of the existing PDG averages [26].

As a cross check we also perform the branching fractions measurements with the subdata set of $88 \times 10^6 B\bar{B}$ pairs that we previously studied [7]. When studying the same decay modes we find values compatible with that of Ref. [7] with both statistical and systematic uncertainties lowered by significant amounts. In addition to the benefit from improved procedures to reconstruct and analyze the data, this updated analysis incorporates new decay modes, higher signal efficiency, and better background rejection and modeling. We use additional control data samples and measure directly in the data the relative ratio of the $B^- \to D^{(*)0}\rho^-$ backgrounds. This analysis employs better fitting techniques and uses more sophisticated methods to combine the results obtained with the various subdecay modes.

VI. POLARIZATION OF $\bar{B}^0 \to D^{*0}\omega$

The polarization of the vector-vector (VV) decay $\bar{B}^0 \to D^{*0}\omega$ has never been measured. Until now, it was supposed to be similar to that of the decay $B^- \to D^{*0}\rho^-$, based on HQET and factorization-based arguments [36]. The angular distributions for the decay $\bar{B}^0 \to D^{*0}\omega$ are described by three helicity amplitudes: the longitudinal H_0 amplitude and the transverse H_+ and H_- amplitudes. In the factorization description of $B \to VV$ decays, the longitudinal component H_0 is expected to be dominant, leading to the fraction of longitudinal polarization, defined as

$$f_L \equiv \frac{\Gamma_L}{\Gamma} = \frac{|H_0|^2}{|H_0|^2 + |H_+|^2 + |H_-|^2}, \tag{17}$$

predicted to be close to unity [3,37–39].

Significant transverse polarizations were measured in $B \to \phi K^*$ (see the review in [26]) and investigated as possible signs of New Physics [40], but could also be the result of nonfactorizable QCD effects [41]. Similar effects were studied in the context of SCET [22], and are expected to arise in the $\bar{B}^0 \to D^{*0}\omega$ decay, in particular, through enhanced electromagnetic penguin decays [42], leading to significative deviation of f_L from unity. It has also been argued in SCET studies that nontrivial long-distance contributions to the $\bar{B}^0 \to D^{*0}\omega$ amplitude may allow a significant amount of transverse polarization of similar size to the longitudinal polarization, leading to a value $f_L \sim 0.5$.

Apart from the motivation of these phenomenological questions, the uncertainty on the angular polarization of $\bar{B}^0 \to D^{*0}\omega$ affects the kinematic acceptance of this decay channel and therefore would be the dominant contribution to the systematic effects for its $\mathcal{B}$ measurement. Hence we measure the fraction of longitudinal polarization for this decay mode. The analysis is performed with $\bar{B}^0 \to D^{*0}\omega$ candidates selected with the same requirements as for the $\mathcal{B}$ analysis described in the previous sections. We consider the subdecays $D^{*0} \to D^0\pi^0$ and $D^0 \to K^-\pi^+$, $K^-\pi^+\pi^0$, $K^-\pi^+\pi^-\pi^+$, and $K^0_S\pi^+\pi^-$.

A. Description of the method

The differential decay rate of $\bar{B}^0 \to D^{*0}\omega$ for the subdecay $D^{*0} \to D^0\pi^0$ is [43]

$$\begin{aligned}\frac{d^3\Gamma}{d\cos\theta_{D^*}\, d\cos\theta_\omega\, d\chi} \propto\ & 4|H_0|^2\cos^2\theta_{D^*}\cos^2\theta_\omega + [|H_+|^2 + |H_-|^2 + 2(\mathrm{Re}(H_+H_-^*)\cos 2\chi - \mathrm{Im}(H_+H_-^*) \\ & \times \sin 2\chi)]\sin^2\theta_{D^*}\sin^2\theta_\omega + (\mathrm{Re}(H_+H_0^* + H_-H_0^*)\cos\chi - \mathrm{Im}(H_+H_0^* - H_-H_0^*)\sin\chi) \\ & \times \sin 2\theta_{D^*}\sin 2\theta_\omega,\end{aligned} \tag{18}$$

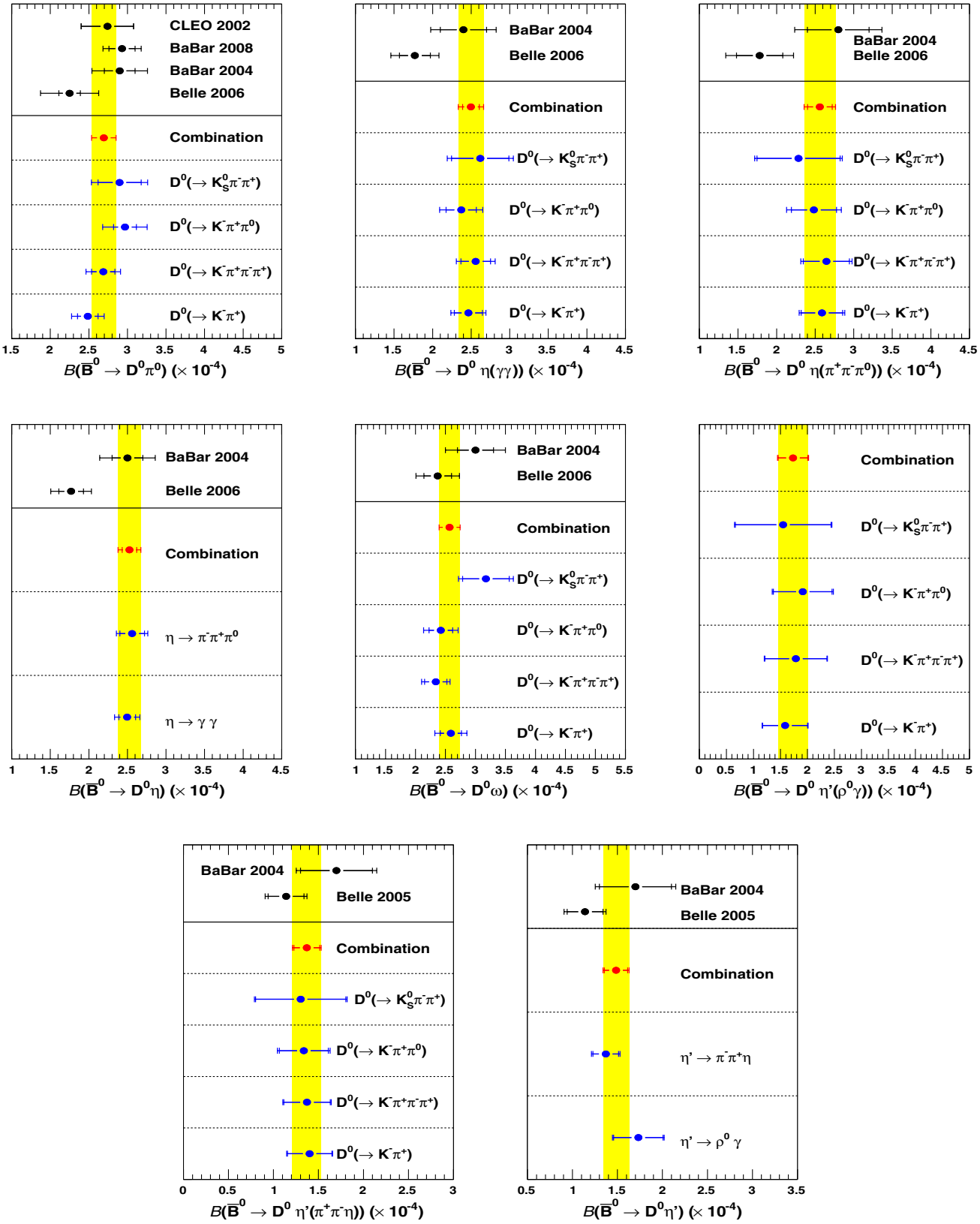

FIG. 5 (color online). $\mathcal{B}(\bar{B}^0 \to D^0 h^0)$ $(\times 10^{-4})$ for the individual reconstructed D^0 and h^0 decay channels (blue points) together with the *BLUE* combination of this paper measurements (vertical yellow bands and the red points). The previous experimental results from *BABAR* [7,14], Belle [11,12], and CLEO [10] are also shown (black points). The horizontal bars represent the statistical contribution alone and the quadratic sum of the statistical and systematic uncertainty contributions. The width of the vertical yellow band corresponds to $\pm 1\sigma$ of the combined measurement, where the statistical and systematic uncertainties are summed in quadrature.

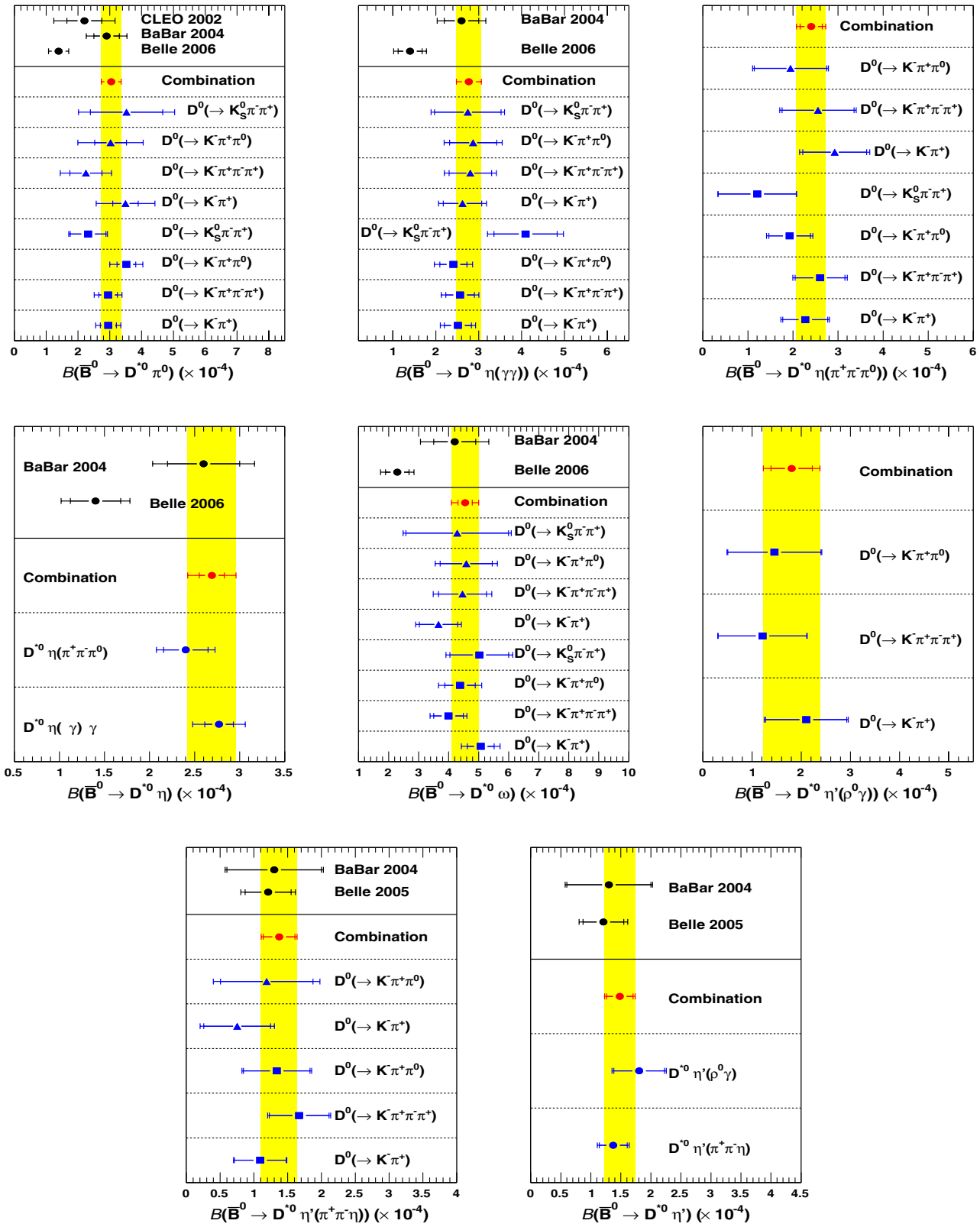

FIG. 6 (color online). $\mathcal{B}(\bar{B}^0 \to D^{*0}h^0)$ ($\times 10^{-4}$) for the individual reconstructed D^0, D^{*0}, and h^0 decay channels together with the *BLUE* combination of this paper measurements (vertical yellow bands and the red points). The blue squares (triangles) are for measurements with the subdecay $D^{*0} \to D^0\pi^0$ ($D^0\gamma$). The previous experimental results from *BABAR* [7,14], Belle [11,12], and CLEO [10] are also shown (black points). The horizontal bars represent the statistical contribution alone and the quadratic sum of the statistical and systematic uncertainty contributions. The width of the vertical yellow band corresponds to $\pm 1\sigma$ of the combined measurement, where the statistical and systematic uncertainties are summed in quadrature.

where θ_{D^*} (θ_ω) is the helicity angle of the D^* (ω) meson (see Sec. III C 3 for definitions). The angle χ, called the azimuthal angle, is the angle between the D^{*0} and ω decay planes in the $\bar{B}^0$ frame. Since the acceptance is nearly independent of χ, one can integrate over χ to obtain a simplified expression:

$$\frac{d^2\Gamma}{d\cos\theta_{D^*} d\cos\theta_\omega} \propto 4|H_0|^2\cos^2\theta_{D^*}\cos^2\theta_\omega + (|H_+|^2 + |H_-|^2)\sin^2\theta_{D^*}\sin^2\theta_\omega. \quad (19)$$

This differential decay width is proportional to

$$4f_L\cos^2\theta_{D^*}\cos^2\theta_\omega + (1 - f_L)\sin^2\theta_{D^*}\sin^2\theta_\omega, \quad (20)$$

which is the weighted sum of purely longitudinal ($f_L = 1$) and purely transverse ($f_L = 0$) contributions.

We employ high statistics MC simulations of exclusive signal samples of $\bar{B}^0 \to D^{*0}\omega$ decays with the two extreme configurations $f_L = 0$ and 1 to estimate the ratio of signal acceptance, $\varepsilon_0/\varepsilon_1$, of $f_L = 0$ events to $f_L = 1$ events. The longitudinal fraction f_L, can be expressed in terms of the fraction of background events (γ) and the fraction of $f_L = 1$ events in the observed data sample (α):

$$f_L = \frac{\alpha}{\alpha + (1 - \alpha - \gamma)\cdot\frac{\varepsilon_0}{\varepsilon_1}}. \quad (21)$$

The fraction γ is taken from the fit of ΔE for a signal region $|\Delta E| < 2.5\sigma_{\Delta E}$ and $m_{\rm ES} > 5.27$ GeV/c^2, where $\sigma_{\Delta E}$ is the fitted ΔE width of the signal distribution, ranging from 20.8 to 23.3 MeV depending on the mode. The fraction α is determined from a simultaneous 2-dimensional fit to the distributions of the helicity angles $\cos\theta_\omega$ and $\cos\theta_{D^*}$, for $\bar{B}^0 \to D^{*0}\omega$ candidates selected in the same signal region. The correlation between $\cos\theta_\omega$ and $\cos\theta_{D^*}$ is found to be negligible.

The signal shapes are described with parabolas (see Eq. (21)), except for the $\cos\theta_\omega$ distribution of $f_L = 0$ signal events, which is described by a nonparametric PDF based on the MC simulation. As the signal distribution of $\cos\theta_\omega$ is distorted around zero because of the selection cut on pion momentum and on the ω boost (see Sec. III B 3). The signal PDF parameters are fixed to those fitted on the $D^{*0}\omega$ simulations. The shape of the $\cos\theta_\omega$ and $\cos\theta_{D^*}$ background distributions is taken from the data sideband $|\Delta E| < 280$ MeV and $5.235 < m_{\rm ES} < 5.270$ GeV/c^2. The consistency of the background shape was checked and validated for various regions of the sidebands in data and generic MC simulations. Possible biases on f_L from the fit are investigated with pseudoexperiment studies for various values of f_L from 5 to 95%. No significant biases are observed.

An additional study is performed with an embedded signal MC simulation, *i.e.* with signal events modeled from various different fully simulated signal samples and with a generated value $f_L \simeq 90\%$ (as expected from HQET [36,44]). A small bias on the fitted value of f_L is observed ($\sim$14% of the statistical uncertainty). This bias is due to the slight difference on the description of the signal shape for the $\cos\theta_\omega$ distribution and for $f_L = 0$, modeled by a nonparametric PDF, and that of the actual shape obtained from the embedded signal MC simulation. This bias is corrected later on and we assign a systematic uncertainty on that correction.

B. Statistical and systematic uncertainties

The statistical uncertainty on f_L is estimated with a conservative approach by varying independently the values of the two fitted parameters α and γ by $\pm 1\sigma$ in Eq. (21). An extended study based on MC pseudoexperiments accounting for the correlations between α and γ gave slightly smaller uncertainty.

The uncertainty due to the signal shape in the simultaneous 2-dimensional fit to $\cos\theta_\omega$ and $\cos\theta_{D^*}$ is measured using the control sample $B^- \to D^{*0}\pi^-$, with $D^{*0} \to D^0\pi^0$ and $D^0 \to K^-\pi^+$. This mode was chosen for its high purity and for its longitudinal fraction $f_L = 1$, which enables us to directly compare its shape to our signal $f_L = 1$. The distribution of the helicity angle of the D^{*0} is found to be wider in the data than in the MC, this difference being parameterized by a parabola. The uncertainty on the signal shape is then measured by refitting α, with the signal PDF being multiplied by the correction parabola. The relative difference is then taken as the uncertainty.

We assign a systematic effect due to the correction that we apply for the observed small bias on the value for f_L, when fitting the embedded signal MC simulation (see the discussion at the end of Sect. VI A).

The uncertainty due to the background shape is measured by refitting α with the background shape fitted in a lower data sideband $|\Delta E| < 280$ MeV and $5.200 < m_{\rm ES} < 5.235$ GeV/c^2. The relative difference is then taken as the uncertainty.

An uncertainty is assigned to f_L due to the assumption of the acceptance being independent of χ. The acceptance of the MC simulation signal is measured in bins of χ and fitted with a Fourier series to account for any deviation from flatness. The resulting fitted function is used as a parametrization of the acceptance dependency to χ and multiplied to the decay rate (as written in Eq. (20)). We then perform in a study based on pseudo-MC simulation experiments where the events are generated from this new decay rate. The resulting $\cos\theta_\omega \times \cos\theta_{D^*}$ distributions are fitted with the procedure described above. A small bias is observed and its value is assigned as a systematic effect.

The uncertainty on the efficiency ratio $\varepsilon_0/\varepsilon_1$, from the limited amount of MC statistics available, is calculated assuming ε_0 and ε_1 to be uncorrelated, while individual uncertainties on ε_0 and ε_1 are calculated assuming a binomial distribution.

TABLE V. Total relative uncertainties computed in data on the measurement of f_L in the decay channel $\bar{B}^0 \to D^{*0}\omega$, with $D^{*0} \to D^0\pi^0$ and $D^0 \to K^-\pi^+$, $K^-\pi^+\pi^0$, $K^-\pi^+\pi^-\pi^+$, and $K^0_S\pi^+\pi^-$.

Sources	$\Delta f_L/f_L(\%)$			
	$K\pi$	$K3\pi$	$K\pi\pi^0$	$K^0_S\pi\pi$
Signal PDFs	2.5	2.9	2.4	2.3
Correction of the bias	1.0	1.3	2.0	2.3
Background PDF	0.3	4.2	3.6	4.0
Limited MC statistics	0.1	0.2	0.3	0.3
Flat acceptance vs χ	1.5	1.8	0.5	6.9
Total systematic	3.1	5.6	4.8	8.6
Statistical uncertainty	9.6	16.3	16.3	25.6
Total uncertainty	10.0	17.2	17.0	27.0

The various relative uncertainties are displayed in Table V for the data and are found to be compatible with those calculated in MC simulations. The dominant uncertainty is statistical. Among the various systematic sources, the largest contribution comes from the signal and background parametrizations, and for some modes on the assumption of a flat acceptance versus χ.

As a check, the f_L measurement is applied in data first on the high purity and high statistics control sample $B^- \to D^{*0}\pi^-$, with $D^{*0} \to D^0\pi^0$ and $D^0 \to K^-\pi^+$. This decay channel is longitudinally polarized, *i.e.* $f_L = 1$. The fit of $\cos\theta_{D^*}$ in data yields a value of f_L compatible with one, as expected.

C. Results for the fraction of longitudinal polarization f_L

The fitted data distributions of the cosine of the helicity angles are given in Fig. 7. The measurements for each D^0 decay channel are then combined with the *BLUE* statistical method [35] (see Sec. V) with $\chi^2/\text{ndof} = 1.01/3$ (*i.e.*: a probability of 79.9%). The measured values of f_L, α, γ and $\varepsilon_0/\varepsilon_1$ are given with the details of the combination in Table VI and in Fig. 8. The final result is $f_L = (66.5 \pm 4.7 \pm 1.5)\%$, where the first uncertainty is statistical and

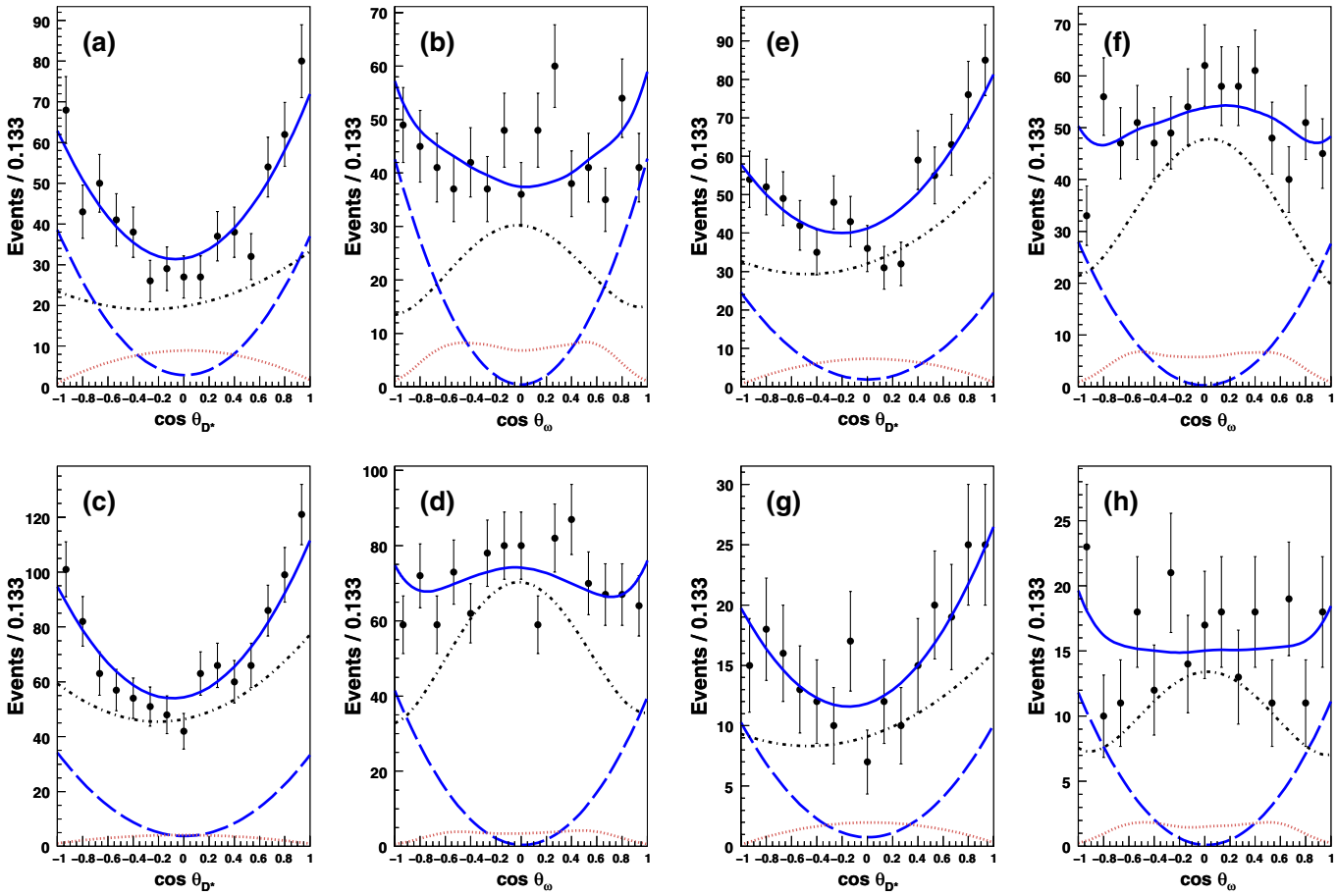

FIG. 7 (color online). Fitted distributions of the helicity $\cos\theta_{D^*}$ and $\cos\theta_\omega$ in the decay channel $\bar{B}^0 \to D^{*0}\omega$ for the D^0 decay modes $K^-\pi^+$ (a) and (b), $K^-\pi^+\pi^0$ (c) and (d), $K^-\pi^+\pi^-\pi^+$ (e) and (f),and $K^0_S\pi^+\pi^-$ (g) and (f). The dots with error bars are data, the curves are the various PDF contributions: the solid blue (blue) is the total PDF, the dash-dot (grey) is the background contribution, the long dash (blue) is the $f_L = 1$ signal part and the dots (red) is the $f_L = 0$ signal.

TABLE VI. Values of α fitted in data, of the background fraction γ and of the acceptance ratio $\varepsilon_0/\varepsilon_1$, with the corresponding values of the longitudinal fraction f_L after the bias correction. The first quoted uncertainty is statistical and the second systematic.

D^0 mode	$\alpha(\%)$	$\gamma(\%)$	$\varepsilon_0/\varepsilon_1$	$f_L(\%)$
$K\pi$	33.4 ± 2.7	52.0 ± 1.9	1.093 ± 0.012	$64.8 \pm 6.5 \pm 2.1$
$K3\pi$	18.8 ± 2.3	71.2 ± 2.5	1.068 ± 0.017	$60.8 \pm 10.3 \pm 3.6$
$K\pi\pi^0$	19.6 ± 2.1	76.0 ± 2.3	1.109 ± 0.021	$76.9 \pm 13.0 \pm 3.8$
$K^0_S\pi\pi$	24.9 ± 4.2	66.0 ± 4.9	1.092 ± 0.016	$66.7 \pm 18.3 \pm 6.2$
Combi.			$f_L = (66.5 \pm 4.7 \pm 1.5)\%$	

the second systematics. This is the first measurement of the longitudinal fraction of $\bar{B}^0 \to D^{*0}\omega$, with a relative precision of 7.4%.

This value differs significantly from the HQET prediction $f_L = (89.5 \pm 1.9)\%$ [36,44]. This significant transverse amplitude in the $\bar{B}^0 \to D^{*0}\omega$ decay channel may arise from the same mechanism as the one that is responsible for the transverse polarization observed in $B \to \phi K^*$. It however supports the existence of effects from nontrivial long-distance contributions to the decay amplitude of $\bar{B}^0 \to D^{*0}\omega$ as predicted by SCET studies [22].

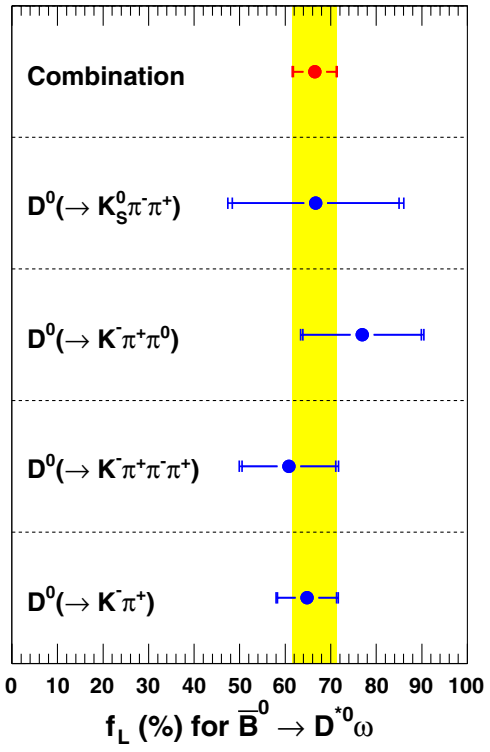

FIG. 8 (color online). Measurements of f_L with the four D^0 modes in data. The yellow band represents the *BLUE* combination.

VII. DISCUSSION

A. Isospin analysis

The isospin symmetry relates the amplitudes of the decays $B^- \to D^{(*)0}\pi^-$, $\bar{B}^0 \to D^{(*)+}\pi^-$ and $\bar{B}^0 \to D^{(*)0}\pi^0$, which can be written as linear combinations of the isospin eigenstates $\mathcal{A}_{I,D^{(*)}}$, $I = 1/2, 3/2$ [5,45],

$$\begin{aligned}
\mathcal{A}(D^{(*)0}\pi^-) &= \sqrt{3}\mathcal{A}_{3/2,D^{(*)}}, \\
\mathcal{A}(D^{(*)+}\pi^-) &= 1/\sqrt{3}\mathcal{A}_{3/2,D^{(*)}} + \sqrt{2/3}\mathcal{A}_{1/2,D^{(*)}}, \\
\mathcal{A}(D^{(*)0}\pi^0) &= \sqrt{2/3}\mathcal{A}_{3/2,D^{(*)}} - \sqrt{1/3}\mathcal{A}_{1/2,D^{(*)}},
\end{aligned} \tag{22}$$

leading to:

$$\mathcal{A}(D^{(*)0}\pi^-) = \mathcal{A}(D^{(*)+}\pi^-) + \sqrt{2}\mathcal{A}(D^{(*)0}\pi^0). \tag{23}$$

The relative strong phase between the amplitudes $\mathcal{A}_{1/2,D^{(*)}}$ and $\mathcal{A}_{3/2,D^{(*)}}$ is denoted as δ for the $D\pi$ system and δ^* for the $D^*\pi$ system. Final state interactions between the states $D^{(*)0}\pi^0$ and $D^{(*)+}\pi^-$ may lead to a value of $\delta^{(*)}$ different from zero and, through constructive interference, to a larger value of $\mathcal{B}$ for $D^{(*)0}\pi^0$ than the prediction obtained within the factorization approximation. One can also define the amplitude ratio $R^{(*)}$,

$$R^{(*)} = \frac{|\mathcal{A}_{1/2,D^{(*)}}|}{\sqrt{2}|\mathcal{A}_{3/2,D^{(*)}}|}. \tag{24}$$

In the heavy-quark limit, the factorization model predicts [46,47] $\delta^{(*)} = \mathcal{O}(\Lambda_{\rm QCD}/m_b)$ and $R^{(*)} = 1 + \mathcal{O}(\Lambda_{\rm QCD}/m_b)$, where m_b represents the b quark mass and where the correction to "1" is also suppressed by a power of $1/N_c$, with N_c the number of colors. SCET [20–22] predicts that the strong phases $\delta^{(*)}$ (ratios $R^{(*)}$) have the same value in the $D\pi$ and $D^*\pi$ systems and significantly differ from 0 (1).

The strong phase $\delta^{(*)}$ can be computed with an isospin analysis of the $D^{(*)}\pi$ system. We use the world average values provided by the PDG [26] for $\mathcal{B}(B^- \to D^{(*)0}\pi^-)$, $\mathcal{B}(\bar{B}^0 \to D^{(*)+}\pi^-)$ and for the B lifetime ratio $\tau(B^+)/\tau(B^0)$. The values of $\mathcal{B}(\bar{B}^0 \to D^{(*)0}\pi^0)$ are taken

TABLE VII. Comparison of the measured branching fractions $\mathcal{B}$, with the predictions by factorization [3,16,49,50] and pQCD [18,19]. The first quoted uncertainty is statistical and the second is systematic.

$\mathcal{B}(\bar{B}^0 \to)(\times 10^{-4})$	This measurement	Factorization	pQCD
$D^0\pi^0$	$2.69 \pm 0.09 \pm 0.13$	0.58 [16]; 0.70 [3]	2.3–2.6
$D^{*0}\pi^0$	$3.05 \pm 0.14 \pm 0.28$	0.65 [16]; 1.00 [3]	2.7–2.9
$D^0\eta$	$2.53 \pm 0.09 \pm 0.11$	0.34 [16]; 0.50 [3]	2.4–3.2
$D^{*0}\eta$	$2.69 \pm 0.14 \pm 0.23$	0.60 [3]	2.8–3.8
$D^0\omega$	$2.57 \pm 0.11 \pm 0.14$	0.66 [16]; 0.70 [3]	5.0–5.6
$D^{*0}\omega$	$4.55 \pm 0.24 \pm 0.39$	1.70 [3]	4.9–5.8
$D^0\eta'$	$1.48 \pm 0.13 \pm 0.07$	0.30–0.32 [50]; 1.70–3.30 [49]	1.7–2.6
$D^{*0}\eta'$	$1.48 \pm 0.22 \pm 0.13$	0.41–0.47 [49]	2.0–3.2

from this analysis. We calculate the values of $\delta^{(*)}$ and $R^{(*)}$ using a frequentist approach [48]:

$$\delta = (29.0^{+2.1}_{-2.6})^\circ, \qquad R = (69.2^{+3.8}_{-3.9})\%, \tag{25}$$

for $D\pi$ final states, and

$$\delta^* = (29.5^{+3.5}_{-4.5})^\circ, \qquad R^* = (67.0^{+4.8}_{-4.7})\%, \tag{26}$$

for $D^*\pi$ final states.

In both $D\pi$ and $D^*\pi$ cases, the amplitude ratio is significantly different from the factorization prediction $R^{(*)} = 1$. The strong phases are also significantly different from zero and are equal in the two systems $D\pi$ and $D^*\pi$ (0° is excluded at 99.998% and 99.750% of confidence level, respectively), which points out that nonfactorizable FSI are indeed not negligible. Those results confirm the SCET predictions.

B. Comparison to theoretical predictions for $\mathcal{B}(\bar{B}^0 \to D^{(*)0}h^0)$

Table VII compares the $\mathcal{B}(\bar{B}^0 \to D^{(*)0}h^0)$ measured with this analysis to the predictions by factorization [3,16,49,50] and pQCD [18,19]. We confirm the conclusion by the previous *BABAR* analysis [7]: the values measured are higher by a factor of about three to five than the values predicted by factorization. The pQCD predictions are closer to experimental values but are globally higher, except for the $D^{(*)0}\pi^0$ modes.

The ratios of the $\mathcal{B}$ are given in Table VIII. It should be noted that the values of these ratios are not computed directly from those quoted in Table IV, as we take advantage of the fact that common systematic uncertainties cancel between D^0h^0 and $D^{*0}h^0$ modes. Therefore the ratios of the $\mathcal{B}$ are first calculated for each subdecays of D^0 and h^0, and then combined with the BLUE method. The ratios $\mathcal{B}(\bar{B}^0 \to D^{*0}h^0)/\mathcal{B}(\bar{B}^0 \to D^0h^0)$ for $h^0 = \pi^0$,

TABLE VIII. Ratios of branching fractions $\mathcal{B}(\bar{B}^0 \to D^{*0}h^0)/\mathcal{B}(\bar{B}^0 \to D^0h^0)$ and $\mathcal{B}(\bar{B}^0 \to D^{(*)0}\eta')/\mathcal{B}(\bar{B}^0 \to D^{(*)0}\eta)$. The first uncertainty is statistical, the second is systematic.

$\mathcal{B}$ ratio	This measurement
$D^{*0}\pi^0/D^0\pi^0$	$1.14 \pm 0.07 \pm 0.08$
$D^{*0}\eta(\gamma\gamma)/D^0\eta(\gamma\gamma)$	$1.09 \pm 0.09 \pm 0.08$
$D^{*0}\eta(\pi\pi\pi^0)/D^0\eta(\pi\pi\pi^0)$	$0.87 \pm 0.12 \pm 0.05$
$D^{*0}\eta/D^0\eta$ (Combined)	$1.03 \pm 0.07 \pm 0.07$
$D^{*0}\omega/D^0\omega$	$1.80 \pm 0.13 \pm 0.13$
$D^{*0}\eta'(\pi\pi\eta)/D^0\eta'(\pi\pi\eta)$	$1.03 \pm 0.22 \pm 0.07$
$D^{*0}\eta'(\rho^0\gamma)/D^0\eta'(\rho^0\gamma)$	$1.06 \pm 0.38 \pm 0.09$
$D^{*0}\eta'/D^0\eta'$ (Combined)	$1.04 \pm 0.19 \pm 0.07$
$D^0\eta'/D^0\eta$	$0.54 \pm 0.07 \pm 0.01$
$D^{*0}\eta'/D^{*0}\eta$	$0.61 \pm 0.14 \pm 0.02$

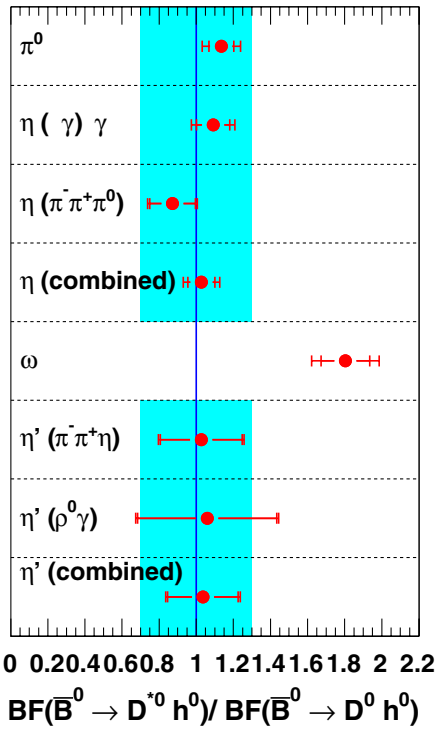

FIG. 9 (color online). Combined ratios $\mathcal{B}(\bar{B}^0 \to D^{*0}h^0)/\mathcal{B}(\bar{B}^0 \to D^0h^0)$ measured in this paper compared to theoretical prediction by SCET [22] (vertical solid line). The vertical band represent the estimated theoretical uncertainty from SCET (for the case where h^0 is the ω meson see text).

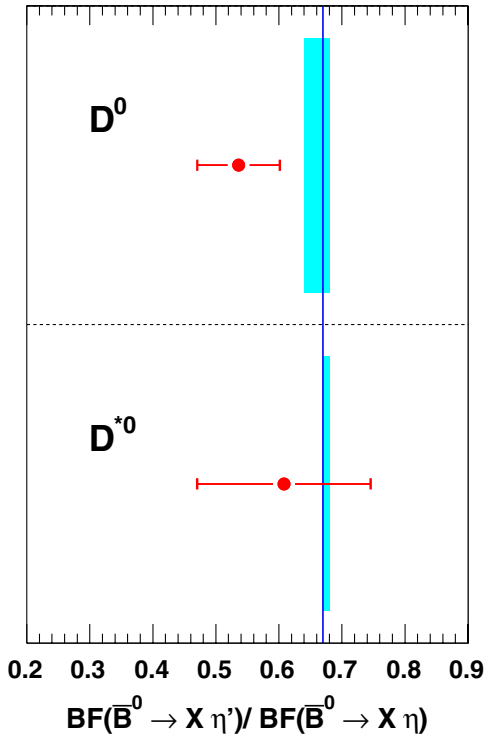

FIG. 10 (color online). Combined ratios $\mathcal{B}(\bar{B}^0 \to D^{*0}\eta')/\mathcal{B}(\bar{B}^0 \to D^{*0}\eta)$ and $\mathcal{B}(\bar{B}^0 \to D^0\eta')/\mathcal{B}(\bar{B}^0 \to D^0\eta)$ measured in this paper compared to theoretical prediction by SCET [22] (vertical line) and from factorization [49] (vertical bands).

η, and η' are compatible with 1. All are displayed in Fig. 9 together with the theoretical predictions.

Factorization predicts the ratio $\mathcal{B}(\bar{B}^0 \to D^{(*)0}\eta')/\mathcal{B}(\bar{B}^0 \to D^{(*)0}\eta)$ to have a value between 0.64 and 0.68 [49], related to the $\eta - \eta'$ mixing. Those ratios are also given in Table VIII and Fig. 10 compares the theoretical predictions with our experimental measurements. The measured ratios are smaller than the predictions and are compatible at the level of less than 2 standard deviations. The SCET gives also a prediction about the ratio $\mathcal{B}(\bar{B}^0 \to D^{(*)0}\eta')/\mathcal{B}(\bar{B}^0 \to D^{(*)0}\eta) \simeq 0.67$, which is similar to the prediction by factorization.

SCET [20–22] does not predict the absolute value of the $\mathcal{B}$ but it predicts that the ratios $\mathcal{B}(\bar{B}^0 \to D^{*0}h^0)/\mathcal{B}(\bar{B}^0 \to D^0h^0)$ are about equal to one for $h^0 = \pi^0$, η and η'. For $h^0 = \omega$ that prediction holds only for the longitudinal component of $\bar{B}^0 \to D^{*0}\omega$, as nontrivial long-distance QCD interactions may increase the transverse amplitude. We measure the fraction of longitudinal polarization to be $f_L = (66.5 \pm 4.7(\text{stat.}) \pm 1.5(\text{syst.}))\%$ in the decay mode $\bar{B}^0 \to D^{*0}\omega$, and find that the ratio $\mathcal{B}(\bar{B}^0 \to D^{*0}\omega)/\mathcal{B}(\bar{B}^0 \to D^0\omega)$ is significantly higher than one, as expected by SCET [22].

VIII. CONCLUSIONS

We measure the branching fractions of the color-suppressed decays $\bar{B}^0 \to D^{(*)0}h^0$, where $h^0 = \pi^0$, η, ω, and η' with $454 \times 10^6 B\bar{B}$ pairs. The measurements are mostly in agreement with the previous results [7,10–12,14] and are the most precise determinations of the $\mathcal{B}(\bar{B}^0 \to D^{(*)0}h^0)$ from a single experiment. They represent significant improvements with respect to the accuracy of the existing PDG averages [26].

For the first time we also measure the fraction of longitudinal polarization f_L in the decay mode $\bar{B}^0 \to D^{*0}\omega$ to be significantly smaller than 1. This reinforces the conclusion drawn from the $\mathcal{B}$ measurements on the validity of factorisation in color-suppressed decays and supports expectations from SCET.

We confirm the significant differences from theoretical predictions by factorization and provide strong constraints on the models of color-suppressed decays. In particular our results support most of the predictions of SCET on $\bar{B}^0 \to D^{(*)0}h^0$ [20–22].

ACKNOWLEDGMENTS

We are grateful for the extraordinary contributions of our PEP-II colleagues in achieving the excellent luminosity and machine conditions that have made this work possible. The success of this project also relies critically on the expertise and dedication of the computing organizations that support *BABAR*. The collaborating institutions wish to thank SLAC for its support and the kind hospitality extended to them. This work is supported by the US Department of Energy and National Science Foundation, the Natural Sciences and Engineering Research Council (Canada), the Commissariat à l'Energie Atomique and Institut National de Physique Nucléaire et de Physique des Particules (France), the Bundesministerium für Bildung und Forschung and Deutsche Forschungsgemeinschaft (Germany), the Istituto Nazionale di Fisica Nucleare (Italy), the Foundation for Fundamental Research on Matter (The Netherlands), the Research Council of Norway, the Ministry of Education and Science of the Russian Federation, Ministerio de Ciencia e Innovación (Spain), and the Science and Technology Facilities Council (United Kingdom). Individuals have received support from the Marie-Curie IEF program (European Union), the A.P. Sloan Foundation (USA) and the Binational Science Foundation (USA-Israel).

[1] H.-Y. Cheng, C.-K. Chua, and A. Soni, Phys. Rev. D **71**, 014030 (2005).
[2] D. Du, Phys. Lett. B **406**, 110 (1997).
[3] M. Neubert and B. Stech, in *Heavy Flavours II*, edited by A. J. Buras and M. Lindner (World Scientific, Singapore, 1998), p. 294.
[4] M. Bauer, B. Stech, and M. Wirbel, Z. Phys. C **34**, 103 (1987).
[5] M. Neubert and A. A. Petrov, Phys. Lett. B **519**, 50 (2001).
[6] A. Deandrea, N. Di Bartolomeo, R. Gatto, and G. Nardulli, Phys. Lett. B **318**, 549 (1993); A. Deandrea *et al.*, *ibid.* **320**, 170 (1994).
[7] B. Aubert *et al.* (*BABAR* Collaboration), Phys. Rev. D **69**, 032004 (2004).
[8] K. Honscheid, K. R. Schubert, and R. Waldi, Z. Phys. C **63**, 117 (1994).
[9] K. Abe *et al.* (Belle Collaboration), Phys. Rev. Lett. **88**, 052002 (2002).
[10] T. E. Coan *et al.* (CLEO Collaboration), Phys. Rev. Lett. **88**, 062001 (2002).
[11] J. Schümann *et al.* (Belle Collaboration), Phys. Rev. D **72**, 011103 (2005).
[12] S. Blyth *et al.* (Belle Collaboration), Phys. Rev. D **74**, 092002 (2006).
[13] A. Kuzmin *et al.* (Belle Collaboration), Phys. Rev. D **76**, 012006 (2007).
[14] B. Aubert *et al.* (*BABAR* Collaboration), Phys. Rev. D **78**, 052005 (2008).
[15] P. del Amo Sanchez *et al.* (*BABAR* Collaboration), Proc. Sci., ICHEP2010 (2010) 250, [arXiv:1007.4464v1] (BABAR-CONF-10/004, SLAC-PUB-14203).
[16] C.-K. Chua, W.-S. Hou, and K.-C. Yang, Phys. Rev. D **65**, 096007 (2002).
[17] L. E. Leganger and J. O. Eeg, Phys. Rev. D **82**, 074007 (2010).
[18] Y. Y Keum, T. Kurimoto, H. Li, C. D. Lü, and A. I. Sanda, Phys. Rev. D **69**, 094018 (2004).
[19] C. D. Lü, Phys. Rev. D **68**, 097502 (2003).
[20] C. W. Bauer, D. Pirjol, and I. W. Stewart, Phys. Rev. D **65**, 054022 (2002).
[21] S. Mantry, D. Pirjol, and I. W. Stewart, Phys. Rev. D **68**, 114009 (2003).
[22] A. E. Blechman, S. Mantry, and I. W. Stewart, Phys. Lett. B **608**, 77 (2005).
[23] C.-K. Chua and W.-S. Hou, Phys. Rev. D **77**, 116001 (2008); R. Fleischer, N. Serra, and N. Tuning, Phys. Rev. D **83**, 014017 (2011); R. Aaij *et al.* (LHCb Collaboration) arXiv:1106.4435 [Phys. Rev. Lett. (to be published)].
[24] M. Gronau, Phys. Lett. B **557**, 198 (2003); M. Gronau, Y. Grossman, N. Shuhmaher, A. Soffer, and J. Zupan, Phys. Rev. D **69**, 113003 (2004); R. Fleischer, Phys. Lett. B **562**, 234 (2003); Nucl. Phys. **B659**, 321 (2003); B. Aubert *et al.* (*BABAR* Collaboration), Phys. Rev. Lett. **99**, 081801 (2007).
[25] B. Aubert *et al.* (*BABAR* Collaboration), Nucl. Instrum. Methods Phys. Res., Sect. A **479**, 1 (2002).
[26] K. Nakamura *et al.* (Particle Data Group), J. Phys. G **37**, 075021 (2010), Mesons section, p. 38.
[27] D. Lange, Nucl. Instrum. Methods Phys. Res., Sect. A **462**, 152 (2001).
[28] T. Sjöstrand, S. Mrenna, and P. Skands, Comput. Phys. Commun. **178**, 852 (2008).
[29] T. Sjöstrand, Comput. Phys. Commun. **82**, 74 (1994).
[30] S. Agostinelli *et al.* (Geant4 Collaboration), Nucl. Instrum. Methods Phys. Res., Sect. A **506**, 250 (2003).
[31] The so-called empirically modified Novosibirsk function divides the fitting region into a peaking region, a low tail region and a high tail region. For a variable x, the modified Novosibirsk function $f(x) = A_p \times \exp(g(x))$, where $g(x)$ is defined, in the peak region $x_1 < x < x_2$, as

$$-\ln 2 \times \left(\frac{\ln(1 + 2\tau\sqrt{\tau^2+1}\frac{x-x_p}{\sigma_p\sqrt{2\ln 2}})}{\ln(1+2\tau^2-2\tau\sqrt{\tau^2+1})}\right)^2,$$

in the low tail region $x < x_1$, as

$$\frac{\tau\sqrt{\tau^2+1}(x-x_1)\sqrt{2\ln 2}}{\sigma_p(\sqrt{\tau^2+1}-\tau)^2\ln(\sqrt{\tau^2+1}+\tau)} + \rho_1\left(\frac{x-x_1}{x_p-x_1}\right)^2 - \ln 2,$$

and in the high tail region $x > x_2$, as

$$-\frac{\tau\sqrt{\tau^2+1}(x-x_2)\sqrt{2\ln 2}}{\sigma_p(\sqrt{\tau^2+1}+\tau)^2\ln(\sqrt{\tau^2+1}+\tau)} + \rho_2\left(\frac{x-x_2}{x_p-x_2}\right)^2 - \ln 2.$$

The parameters are: i) A_p is the value at the maximum of the function, ii) x_p is the peak position, iii) σ_p is the width of the peak defined as the width at half-height divided by $2\sqrt{2\ln 2} \simeq 2.35$, iv) τ is an asymmetry parameter. v) $\rho_{1/2}$ described the width of the respective tails. The positions $x_{1,2}$ are $x_p + \sigma_p\sqrt{2\ln 2}(\frac{\xi}{\sqrt{\xi^2+1}} \mp 1)$. Left and right tails are attached to the peak with the conditions of continuity and first derivative.
[32] J. C. Anjos *et al.* (E691 Collaboration), Phys. Rev. D **48**, 56 (1993).
[33] A. Höcker *et al.* (TMVA Group), CERN Report No. CERN-OPEN-2007-007, 2007.
[34] S. M. Berman and M. Jacob, Phys. Rev. **139**, B1023 (1965).
[35] L. Lyons, D. Gibaut, and P. Clifford, Nucl. Instrum. Methods Phys. Res., Sect. A **270**, 110 (1988); B. Aubert *et al.* (*BABAR* Collaboration), Phys. Rev. D **78**, 112003 (2008).
[36] S. E. Csorna *et al.* (CLEO Collaboration), Phys. Rev. D **67**, 112002 (2003).
[37] A. R. Williamson, in *Proceedings of the 4th Flavor Physics and CP Violation Conference, Vancouver, British Columbia, Canada*, FPCP06, eConf C060409 (2006).
[38] J. G. Koerner and G. R. Goldstein, Phys. Lett. B **89**, 105 (1979).
[39] B. Aubert *et al.* (*BABAR* Collaboration), Phys. Rev. Lett. **92**, 141801 (2004).
[40] P. K. Das and K. C. Yang, Phys. Rev. D **71**, 094002 (2005). Y. D. Yang; R. Wang and G. R. Lu, Phys. Rev. D **72**, 015009 (2005); C. S. Huang, P. Ko, X. H. Wu, and Y. D. Yang, Phys. Rev. D **73**, 034026 (2006); B. Aubert *et al.* (*BABAR* Collaboration), Phys. Rev. D **78**, 092008 (2008).
[41] H. Y. Cheng, C. K. Chua, and A. Soni, Phys. Rev. D **71**, 014030 (2005).
[42] M. Beneke, J. Rohrer, and D. Yang, Phys. Rev. Lett. **96**, 141801 (2006).

[43] G. Kramer and W. F. Palmer, Phys. Rev. D **45**, 193 (1992).

[44] J. L. Rosner, Phys. Rev. D **42**, 3732 (1990); M. Neubert, Phys. Lett. B **264**, 455 (1991); G. Kramer, T. Mannel, and W. F. Palmer, Z. Phys. C **55**, 497 (1992); J. D. Richman, *Heavy Quark and CP Violation, in Probing the Standard Model of Particle Interactions*, edited by R. Gupta, A. Morel, E. De Rafael, and F. David Les Houches Session LXVIII, 1997 (Elsevier, Amsterdam, 1999).

[45] J. L. Rosner, Phys. Rev. D **60**, 074029 (1999).

[46] M. Beneke, G. Buchalla, M. Neubert, and C. T. Sachrajda, Nucl. Phys. **B591**, 313 (2000).

[47] H.-Y. Cheng and K.-C Yang, Phys. Rev. D **59**, 092004 (1999).

[48] J. Charles *et al.* (CKMfitter group), Eur. Phys. J. C **41**, 1 (2005).

[49] A. Deandrea and A. D. Polosa, Eur. Phys. J. C **22**, 677 (2002).

[50] J. O. Eeg, A. Hiorth, and A. D. Polosa, Phys. Rev. D **65**, 054030 (2002).